Deutsches Zentrum für Luft- und Raumfahrt
German Aerospace Center

FH AACHEN UNIVERSITY OF APPLIED SCIENCES

Master Thesis

CFD Simulation of Airflow in a New Receiver Concept for High-Temperature Solar Heating

By

Oguzhan Nohutcu

Department of Aerospace Engineering

Aachen University of Applied Sciences, Aachen

2023

Supervised By

Prof. Dr.-Eng. Daniel Grates

Prof. Dr.-Eng. Andrii Cheilytko

CFD Simulation of Airflow in a New Receiver Concept for High-Temperature Solar Heating

A THESIS SUBMITTED IN THE PARTIAL FULFILLMENT OF THE REQUIREMENTS FOR THE DEGREE OF MASTER OF SCIENCE IN AEROSPACE ENGINEERING

Declaration

I "Oguzhan Nohutcu" hereby solemnly declare that this thesis titled, "CFD Simulation of Airflow in a New Receiver Concept for High-Temperature Solar Heating" is my own work and that I have not used any sources other than those listed in the bibliography. Content from published or unpublished works that has been quoted directly or indirectly or paraphrased is indicated as such. The thesis has not been submitted in the same or similar form for any other academic award. The electronic version I have submitted is completely identical to the hard copy version submitted.

Dedication

I would like to take this opportunity to thank all those who have supported me in the preparation of this thesis. First of all, I would like to thank Prof. Dr.-Eng. Andrii Cheilytko for his supervision and for making it possible for me to work at the DLR Instute of Solar Research on such an interesting topic and for all of the resources and support he provided. I would also like to thank Prof. Dr.-Eng. Daniel Grates for his invaluable guidance and support throughout my master's program. Their expertise and encouragement helped me to complete this research and write this thesis. A special thanks to my family for their love and support during this process. Without them, this journey would not have been possible.

Abstract

Open cavity solar receivers play an important role in concentrated solar power (CSP) systems and hold great promise, particularly in scenarios where their ability to absorb high fluxes at very high temperatures yields beneficial results. This intense concentration of sunlight can be used to produce electricity through various means, such as generating steam to drive a turbine. The efficiency of the open volumetric receiver concept relies heavily on the air return ratio (ARR) which refers to the proportion of air recirculated and returned to the receiver. A high ARR contributes to high receiver efficiencies, as with rising ARR, the reused part of the enthalpy of warm air increases. This paper deals with the design and simulation of a new receiver concept with a conical cavity and square cross-section. The objective is to identify the most effective design arrangement for the square-cone structure, considering different depths, that maximizes both the air return ratio (ARR) and thermal efficiency. The findings demonstrate that increasing the depth of the mentioned receiver leads to a rise in the ARR, up to a certain threshold which can reach values up to 94,53 %, beyond which there is a subsequent decline in efficiency. Furthermore, this study examined how varying the amount of air passing through a specific section of the receiver across a defined area, along with the temperature changes in these sections, affected its operational efficiency.

Contents

List of Tables

List of Figures

Nomenclature

Greek Characters

Symbol	Description	Unit
μ	dynamic viscosity	$\frac{\mathrm{kg}}{\mathrm{m \cdot s}}$
ϕ	irradiation	$-$
ρ	density	$\frac{\mathrm{kg}}{\mathrm{m}^3}$
ξ	passive scalar	$-$

Latin Characters

Symbol	Description	Unit
f_b	body force	N
C	Celcius	$\circ$
x, y, z	coordinates in the cartesian coordinate system	$-$
$\dot{Q}_S$	heat flow across surface	$\frac{\mathrm{J}}{\mathrm{s}}$
$\dot{Q}_V$	heat generated or destroyed inside the volume	$\frac{\mathrm{J}}{\mathrm{s}}$
K	Kelvin	$\circ$
$\dot{m}$	mass flow	$\frac{\mathrm{kg}}{\mathrm{s}}$
m	mass	kg
p	pressure	Pa
Sc	Schmidt-Number	m
f_S	surface force	N
t	time	t
u	velocity component in x-direction	$\frac{\mathrm{m}}{\mathrm{s}}$
v	velocity	$\frac{\mathrm{m}}{\mathrm{s}}$
u,v,w	velocity components in x,y,z	$\frac{\mathrm{m}}{\mathrm{s}}$
$\vec{u}$, $\vec{v}$, $\vec{w}$	mean velocity components in x,y,z	$\frac{\mathrm{m}}{\mathrm{s}}$
V	volume	m^3
W	work	J

Abbreviations

Acronym	Description
ARR	air return ratio
$CATIA$	CATIA CAD software
CFD	computational fluid dynamics
$CIEMAT$	Centro de Investigaciones Energeticas, Medioambientales y Tecnologicas
CSP	concentrated solar power
DLR	Deutsches Zentrum für Luft und Raumfahrt
DNI	direct normal irradiance
DNS	Direct Numerical Simulation
$GCON$	general connectivity
$HiTRec$	high temperature receiver
HTF	heat transfer fluid
IEA	International Energy Agency
$IRENA$	International Renewable Energy Agency
LES	large eddy simulation
LFR	linear fresnel reflector
OVR	open volumetric receiver
PV	photovoltaic
$RANS$	Reynolds averaged Navier-Stokes equation
STE	solar thermal energy
STJ	solar tower Jülich
$VoCoRec$	volumetric conical receiver

1 Introduction

The current trends in energy generation are economically, ecologically and socially unsustainable. As the world strives to transition to sustainable energy sources, the importance of utilising renewable energy is becoming increasingly evident. Sustainable and low-carbon energy technologies will play an essential role in the energy transition energy revolution needed to halt climate change. Among various renewable energy technologies, concentrated solar power (CSP) stands out as a promising and versatile solution. Harnessing the power of the sun, CSP offers numerous advantages that make it an attractive option for our future energy needs. Considering these advantages, International Energy Agency (IEA) aims for the share of solar thermal electricity in global electricity generation to reach 11% by 2050. Although photovoltaic (PV) technology has already established itself in the energy market, solar thermal energy (STE) technology will have a significant long-term role due to its inherent storage capabilities. These capabilities enable CSP plants to produce energy on demand. This advantage will become even more crucial as variable renewable energy sources like PV and wind power increase their share in global electricity generation.

Conventional surface receivers are widely utilized in operational CSP plants across the globe. However, their thermal efficiency is restricted due to significant heat dissipation during the transfer of heat between the absorbing surface and the heat transfer fluid. Additionally, their absorption area is limited to two dimensions. Consequently, efforts in research have also been directed towards the advancement of volumetric receivers, which can directly or indirectly capture concentrated solar radiation in three dimensions. These receivers are considered the most favorable substitute for tubular receivers.

Cavity receivers, owing to their minimal radiation losses, emerge as a promising solution for high-temperature applications in solar towers. By utilizing more advanced components and minimizing losses in heat transfer, CSP systems can produce electricity with greater efficiency. This thesis focuses on examining various design strategies for cavity air receivers with the goal of attaining a high air return ratio, ultimately leading to increased efficiency.

1.1 Solar Thermal Energy

Research has shown that available solar energy accounts for more than 90% of renewable energy resources, showing the potential for its use. Solar thermal energy (STE) refers to the utilization of solar radiation to generate heat or thermal energy. STE generates electricity without producing greenhouse gas emissions, so it can be a key technology for mitigating climate change. Solar thermal systems typically involve the use of solar collectors or mirrors (heliostats) to concentrate sunlight onto a receiver, which absorbs the solar radiation and converts it into thermal energy. Unlike PV technology, which converts sunlight directly into electricity, solar thermal energy focuses on capturing and utilizing the Sun's heat for various applications. These plants can also store the extracted heat to convert it into electricity later on, which is a great benefit when there is a need for electricity, when clouds block the sun, or after sunset.[22].

By the end of 2015, the leader of the total capacity in operation installed in was China (309.5 GW_{th}) which is followed by Europe (49.2 GW_{th}). The worldwide solar thermal capacity witnessed substantial expansion, escalating from 62 GW_{th} (equivalent to 89 million square meters) in 2000 to 456 GW_{th} (equivalent to 652 million square meters) by 2016 [29].

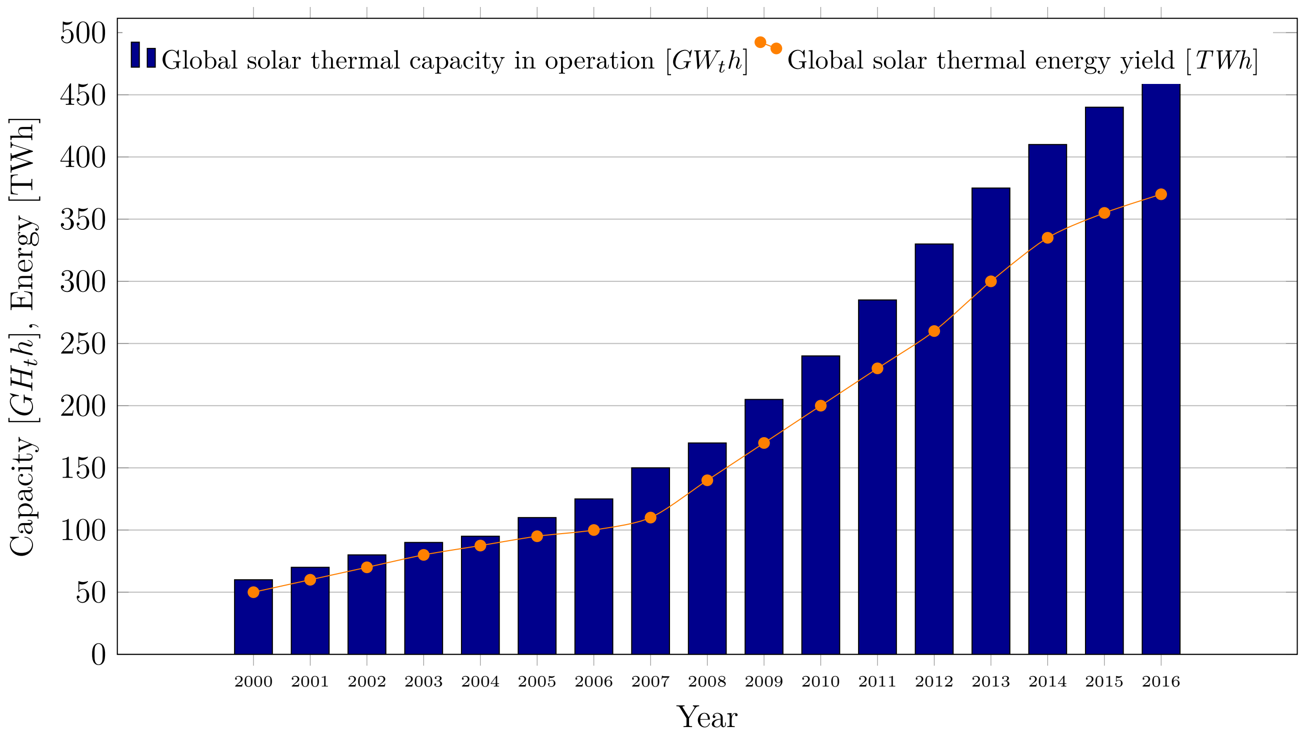

Figure 1: Global solar thermal capacity and solar thermal energy distribution
Source: Solar Heat Worldwide, 2020

1.1.1 Solar Irradiance

The solar irradiance is the measurement of the amount of light energy emitted by the Sun's entire disk and received at the Earth in watts per square meter (W/m^2) using SI units. The Sun emits energy in the form of photons, energetic particles, and magnetic fields. Each of these components has a noticeable effect on Earth or its surroundings. Photons follow a direct path from the Sun to Earth, encompassing a range of wavelengths spanning from high-energy X-rays and gamma rays to visible light, infrared, and radio waves. This property can be measured for any source of light, such as stars, the moon, or even everyday sources like the bright headlights of an oncoming vehicle.

The amount of energy that reaches the surface is $1kW/m^2$ under clear conditions when the Sun is close to the zenith. It can be differentiated into two components: direct beam radiation and diffuse radiation. Diffuse radiation comes indirectly after being scattered in all directions by the atmosphere, and direct beam radiation comes straight from the Sun. For concentrated radiation on smaller devices, only direct normal irradiance (DNI) is relevant. This measurement is taken on surfaces that are perpendicular to the Sun's rays. Moreover, a portion of the solar energy that reaches the Earth is lost as it travels through the atmosphere for several reasons. Some of it is reflected back into space by clouds and aerosols. This reflection happens because of factors such as the increased air mass, the angle at which the rays hit the Earth's surface, and the albedo effect. The quality of the DNI is crucial for CSP power plants, as below a certain value, the net output of such a power plant would be zero. DNI is commonly found in hot and dry regions with clear skies and a low aerosol rate. These areas typically fall within subtropical latitudes, approximately between 15° to 40° north or south.

1.1.2 Concentrated Solar Power

In recent years, the concentrated solar power (CSP) sector has become increasingly promising as a technology for generating solar energy. This is mainly due to its ability to facilitate large-scale energy production. The reason behind this phenomenon are apparent: the Sun serves as an infinite resource for power generation, offering not only a cost-free fuel but also an entirely emissions-free source.

CSP achieves solar energy generation by directing mirrors or lenses to concentrate a substantial expanse of sunlight onto a collector. Within this collector, a fluid or other medium that conveys heat undergoes heating. Concentrated sunlight is used to generate heat, which is then used to power a heat engine, usually a steam turbine, that is connected to an electric generator or causes a thermochemical reaction [21].

According to International Renewable Energy Agency (IRENA) in 2016, the total installed capacity of solar-thermal power plants across the globe has reached approximately 6.4 GW, representing an almost five-fold increase on 2010.

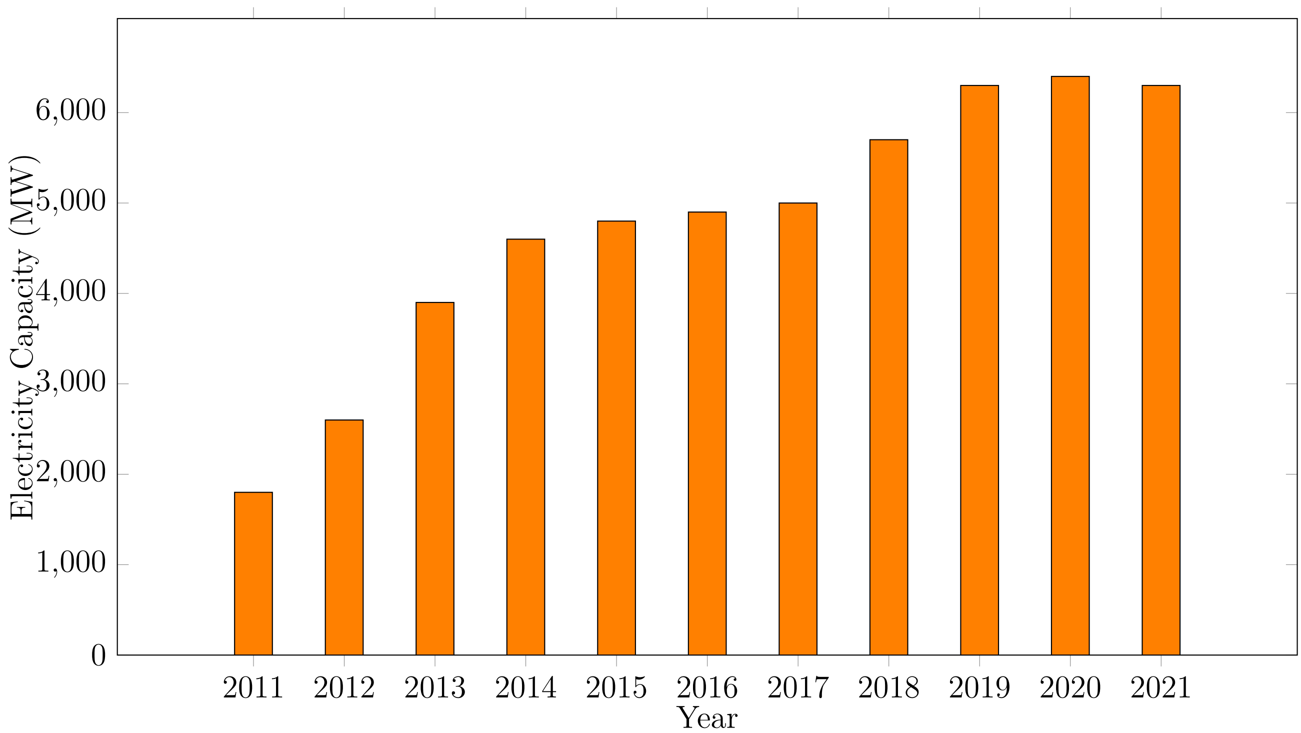

Figure 2: Electricity Capacity Trends
Source: IRENA, 2022

Four distinctive types of CSP technologies are prevalent: linear Fresnel reflector, solar tower, parabolic dish, and parabolic trough. Each of these technologies has its own set of advantages and considerations in terms of efficiency, scalability, and applicability to different geographic locations and environmental conditions. Decisions regarding the implementation of technology are often influenced by factors such as the amount of land space available, the availability of resources like sunlight, and the project budget.

1.1.3 Linear Fresnel Reflector

The linear Fresnel reflector (LFR) design includes a configuration of linear arrays of mirrors that concentrate the beam radiation onto a linear receiver tube. Furthermore, a flat or gently curved secondary reflector is used to cover the top part of the absorber tube, which helps to increase the concentration of solar radiation. LFR systems are composed of sequences of slender mirror segments that are aligned to redirect sunlight towards a stationary receiver located at the focal point of the reflectors. Each set of LFR has its own solar tracking mechanism and is fine-tuned individually to ensure that sunlight is consistently concentrated onto the stationary receiver.

The receiver in this configuration consists of a long absorber tube that is coated with a selective material. The concentrated solar energy is transferred to the receiver, which contains a heat-transfer fluid that can remain in liquid form even at high temperatures. This heated fluid then increases the temperature of water using a heat exchanger, which helps generate steam. Due to their structural design, LFR systems are highly modular and can be manufactured and assembled cost-effectively in solar fields of different sizes. While LFR tends to have slightly lower optical efficiency, it can offer potential cost savings.

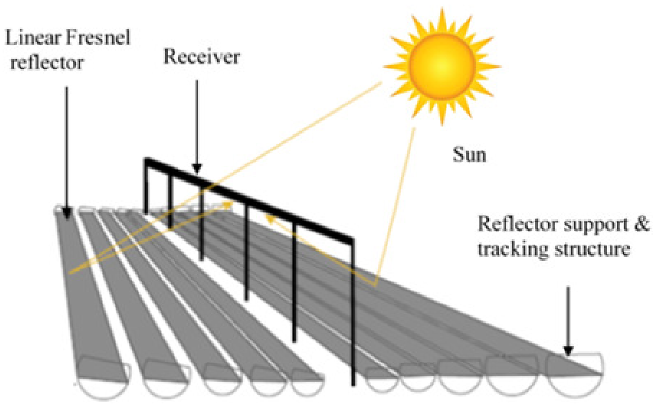

Figure 3: Linear Fresnel Reflector
Source: Solar energy: direct and indirect methods to harvest usable energy [20]

1.1.4 Parabolic Dishes

Parabolic-dish solar concentrators are advanced solar tracking mechanisms that can adjust along two axes. They redirect sunlight and concentrate it onto a thermal receiver positioned at the focal point of the dish collector. These collectors consist of a configuration of mirrors that are shaped like parabolic dishes [12]. The described systems utilize a collection of these parabolic mirrors. Concentrators operate at temperatures above 1800 Kelvin, with concentration ratios typically ranging from 1000 Kelvin to 5000 Kelvin. Solar parabolic-dish concentrating systems are ideal for concentrated photovoltaic applications because they have high concentration ratios and can operate at high temperatures. Despite their exceptional optical efficiency, it remains challenging to mitigate the substantial expenses and associated risks of this technology. Storing the generated heat is a significant challenge.

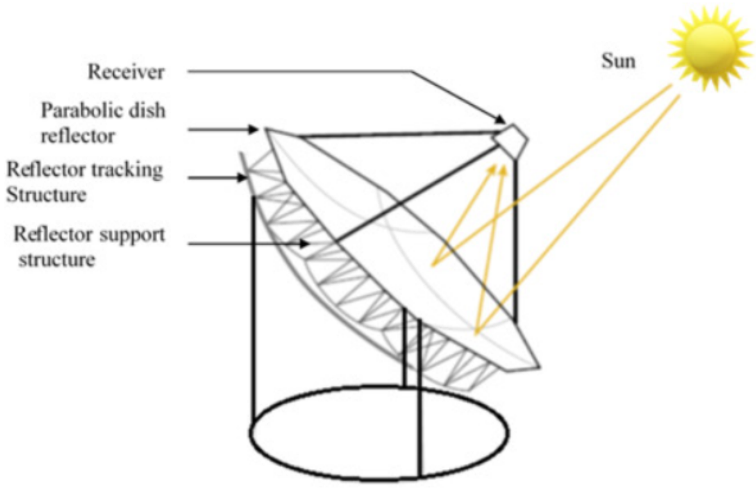

Figure 4: Parabolic Dish
Source: Solar energy: direct and indirect methods to harvest usable energy [20]

1.1.5 Parabolic Through

A parabolic trough solar facility employs elongated, trough-like solar concentrators to gather solar energy and direct it towards a linear heat receiver. These reflective devices follow the Sun's path to optimize their effectiveness. In a similar vein, the Fresnel collection system closely resembles the parabolic trough design by utilizing lengthy, flat mirrors capable of Sun tracking as well [3]. The Fresnel system closely resembles the parabolic trough design by utilizing lengthy, flat mirrors capable of Sun tracking as well.

Parabolic-trough solar concentrators represent an advanced and feasible method for harnessing solar energy for industrial applications. These systems operate within the temperature range of 500–700K.

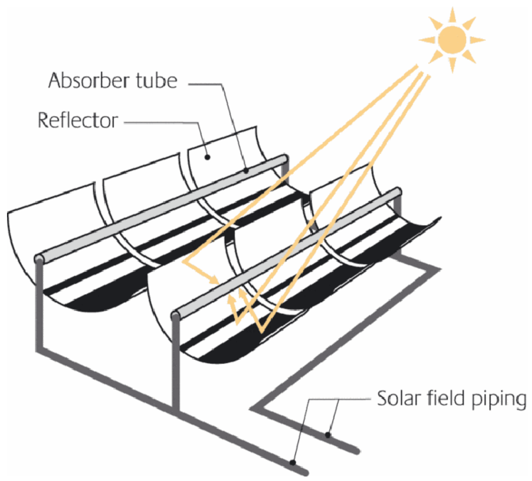

Figure 5: Parabolic Through
Source: concentrated solar power plants [13]

1.1.6 Solar Tower Plant

In a solar tower power plant setup, multiple mirrors (heliostats) redirect solar radiation towards a central receiver located on a tower structure. These mirrors can be either flat or curved. However, flat mirrors that can track the movement of the Sun are generally preferred because they are cheaper than curved mirrors. As these mirrors track the Sun's path, they efficiently capture the incoming sunlight and redirect it towards the solar tower. A large number of these mirrors work together to concentrate a significant amount of solar radiation onto a specific spot on the tower, known as the receiver. The receiver holds paramount importance within the plant, as it absorbs the intensified solar radiation and transfers it to a heat transfer fluid (HTF). This fluid helps transfer heat from sunlight to water. Among the various concentration technologies available, tower systems are considered to be the second most favorable option, with parabolic dishes ranking first. Tower systems have the potential to greatly reduce costs in the future[11].

The Ivanpah Solar Electric Generating System stands as the largest concentrated solar thermal plant USA. Situated in the Mojave Desert, this facility is able to generate 392 MW of electricity. It accomplishes this by using 173,500 heliostats, each equipped with two mirrors that concentrate sunlight onto three solar power towers. Beyond the United States, Spain is home to several power tower installations. The Planta Solar 10 and Planta Solar 20 systems, employ water/steam setups with capacities of 11 and 20 MW, respectively. The solar tower in Jülich, Germany, has an electricity production capacity of 1.5 MW, with the assistance of over 2000 installed heliostats.

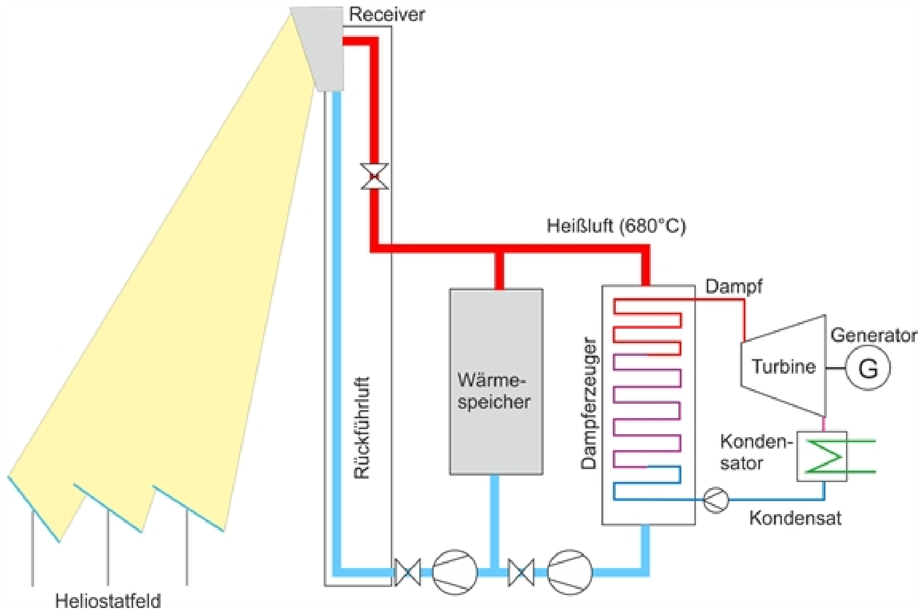

Figure 6: Illustration of a power plant with an open volumetric receiver
Source: DLR [26]

The process scheme of a solar tower power plant with an open volumetric air receiver is illustrated in Figure 6. The incident direct solar radiation is focused onto the receiver at the top of the solar tower using an array of mirrors called heliostats. The primary objective of the receiver is to capture the concentrated solar irradiation and transfer the heat to a transfer medium, typically air, at the highest possible temperatures. These temperatures can range from 700°C to over 1000°C. The heated air has two purposes: it either generates steam for the turbine or is stored in thermal energy storage systems. The steam generation system consists of a heat exchanger that absorbs heat from the air to produce steam, a steam turbine that converts thermal energy into mechanical power, and a generator that ultimately delivers the electricity to the transformer for distribution. After passing through the thermal energy storage, the air is returned to the receiver to reuse its heat. This recirculated air also helps cool the metal support structure, preventing the occurrence of overheating problems. Upon exiting the individual absorber modules, the air is blown out, causing it to mix with the surrounding air. Only a fraction of the air that is returned is drawn back into the system. The air flowing through each absorber module is heated to the specified ambient temperature, T_{abs} [24].

1.2 Open Volumetric Air Receivers

Various receiver technologies are being employed and studied in the field of solar tower plants. These receivers can be distinguished by the medium they use for heat transfer. Volumetric receivers generally use substances like molten salt, steam, particles, or air for this purpose [9].

Open volumetric air receivers (OVARs) contribute to a more sustainable energy landscape. They offer an alternative to the commonly used molten salt and steam receivers in various applications. Open volumetric air receivers present various advantages when compared to the current systems. In comparison to molten salt setups, open volumetric receivers are less complex technically and allow for straightforward integration of heat storage. Unlike steam receivers, these offer more durability during temporary operations and can handle higher process temperatures, exceeding 650 °C. As a result, open volumetric receivers are not only attractive for electricity generation but also hold potential for chemical and industrial processes. Benefits of using air as the heat transfer fluid are:

- Cost-effective
- Readily available
- Non-toxic
- Not limited by temperature constraints

Certain challenges still exist in implementing open volumetric receivers. Factors like thermal efficiency, durability of the absorber material, and costs should be addressed and optimized, depending on the specific design used.

In summary, open volumetric air receivers present a promising alternative to existing molten salt and steam receiver systems. They provide technical simplicity, easy integration of heat storage and the ability to reach high process temperatures. While challenges exist, such as thermal efficiency and material durability, open volumetric receivers hold significant potential for various industrial applications [7].

DLR began researching open volumetric receivers in 1996, with a focus on studying potential absorber materials. This effort resulted in the development of the high temperature receiver (HiTRec), which is a type of open volumetric receiver (OVR) technology. The HiTRec in Figure 7 is a volumetric receiver design that was developed in the 1990s and 2000s by the collaboration between Deutsches Zentrum für Luft und Raumfahrt (DLR) and Centro de Investigaciones Energeticas, Medioambientales y Tecnologicas (CIEMAT). This design has been continuously developed and refined. One notable characteristic of this technology is that the front side of the receiver comprises numerous identical modules featuring a ceramic volumetric absorber grid. A significant milestone in the advancement of the HiTRec technology occurred with the construction and activation of the STJ. This research and demonstration power plant, boasting a capacity of 1.5 $MWel$, began operation in 2008, and the first electricity was successfully integrated into the grid in early 2009.

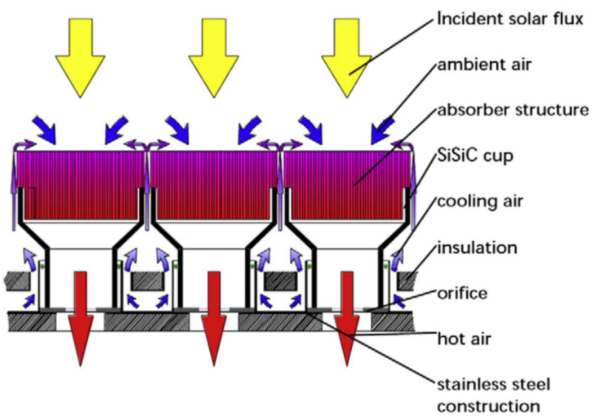

Figure 7: Scheme of HiTRec receiver design
Source: DLR [26]

One drawback of this concept is the requirement for airflow to cool the support structure of the modules. Recent years have witnessed substantial advancements in improving the HiTRec receiver concept. Given the high temperatures ranging from 700-1000 °C in solar thermal towers, notable thermal losses are anticipated in the receiver. Effectively managing these thermal losses in the receiver is essential for improving the overall performance of the system. In this regard, the notion of employing a cavity to mitigate radiation losses emerged in previous decades, exerting a substantial impact on controlling radiative losses. However, the convective losses still need to be considered. This modification aims to improve the ARR and reduce radiation losses, ultimately leading to higher receiver efficiencies [16]. One of these designs is called the volumetric conical receiver (VoCoRec). The VoCoRec is a receiver concept with modular design. Each module is an open cavity with a conical inner shape and a hexagonal cross-section (Figure 8).

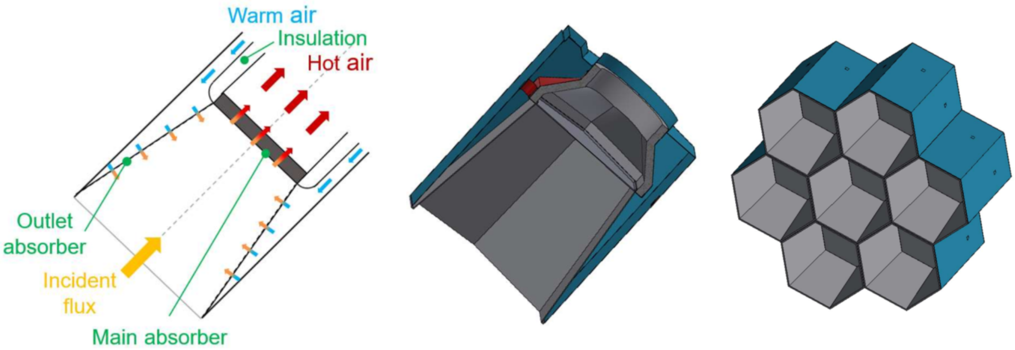

Figure 8: VoCoRec Design
Source: DLR [26]

The absorber surfaces exposed to solar irradiation consist of multiple layers of metal wire mesh, allowing air to pass through and undergo a two-stage heating process. During the initial stage, the air, initially at around 100 °C, flows through an outlet absorber that is exposed to radiation and enters the cavity. Subsequently, in the second stage, the preheated air is drawn through the primary absorber. This process results in the air being heated to its ultimate temperature of approximately 700 to 800 °C.

The design of the cavity offers a significant advantage in achieving high ARR and reducing radiation losses compared to external receivers. The two-stage heating process helps to minimize radiation losses by keeping the material temperatures lower. Additionally, the efficient separation of hot and warm air through effective insulation aids in achieving high temperatures. The cooling needs for the supporting structure are also relatively minimal. The use of metal wire mesh as the absorbing material helps to decrease the specific investment costs. A new cavity design project is currently in progress. The project aims to simplify construction, lower costs, and enhance ARR efficiency. To improve the geometric design in terms of efficiency several analyses will be conducted in the following chapters of this thesis.

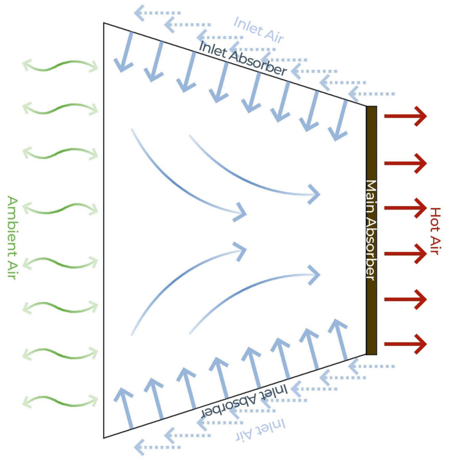

(a) Receiver flow map

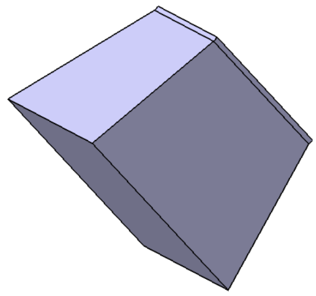

(b) Receiver CAD model

Figure 9: Illustration of the new receiver concept

Figure 9 depicts the basic layout of the new receiver concept, which has a modular receiver design. Each receiver module is constructed as an open cavity with an inner square-cone shape. In the illustrated model, air at 450°C enters the cavity through the inlet absorber with a mass flow rate of 0.07 kg/s. Inside the cavity, the air goes through a heating process until it reaches its eventual temperature of roughly 700°C.

The primary goal of this thesis is to define the most effective design for the square-cone shaped receiver mentioned, with the aim of maximizing its performance. To achieve this, computational fluid dynamics (CFD) simulations were carried out using ANSYS CFX for different configurations with differing aperture depths. These simulations were conducted to establish the ARR ultimately identifying which configuration offers the greatest efficiency and compliance. In the second part of the thesis, an examination of the dependencies of the ARR on the mass flow gradient and temperature gradient on the absorber will be analyzed.

1.2.1 Air Return Ratio

The air return ratio in an open volumetric air receiver refers to the proportion of air that is recirculated and returned to the receiver. It represents the fraction of air that is redirected back into the system after being expelled or discharged (Equation 1.1). Specifically, a high air return ratio is particularly important when higher return air temperatures yield beneficial outcomes. A high ARR contributes to high receiver efficiencies as with rising ARR values the reused part of the warm air's enthalpy rises. A high ARR holds vital importance in maximizing receiver efficiency, especially when high return air temperatures are advantageous for subsequent processes. As studies conducted by Marcos et al. (2004) [16] emphasize the significance of the ARR in enhancing the receiver's efficiency.

$$ARR = \frac{\dot{m}_{\text{ReturnedInletAir}}}{\dot{m}_{\text{HotAir}}} \tag{1.1}$$

At the STJ, Tiddens [27], carried out measurements of the ARR using a tracer gas method. Helium gas was added to the recirculated hot air at a fixed concentration before it left the receiver. In the hot air tube behind the receiver, a measurement was then made of the helium that had reached there. From the change in concentration, the ARR could then be calculated. Numerically, the ARR can be determined by solving the transport equation (Equation 1.2) for a passive scalar ξ following the flow simulation. The scalar ξ is thereby restricted to values between zero and one, thus it forms the concentration of the Helium gas from the tracer gas method [2].

$$\frac{\partial}{\partial t}(\rho\xi) + \nabla \cdot (\rho\vec{U}\xi) - \nabla \cdot \left(\frac{\mu}{Sc}\nabla\xi\right) = 0 \tag{1.2}$$

The transport equation is solved according to the flow simulation, so ρ is the air density, $\vec{U}$ the speed and µ is the dynamic viscosity of the air. The Schmidt number Sc characterizes the relationship between diffusive momentum and mass transport and is taken as one here. The air recirculation rate can be calculated using mass flow-weighted averaging

$$ARR = \frac{\sum_{k\in M_{Abs}} (\xi_k \cdot \dot{m}_k\,(1-\gamma_k))}{\sum_{k\in M_{Abs}} (\dot{m}_k\,(1-\gamma_k))} \tag{1.3}$$

Optimizing the air return ratio is essential for maximizing the efficiency of the CSP system. This ensures that the heated air is efficiently used to generate power before being cycled back for reheating. This contributes to higher overall energy conversion efficiency in the CSP plant.

2 Theory

This section covers the theory behind fluid flow and CFD equations as well as the different turbulence models and their implementation employed in this thesis.

2.1 Fluid Flow Theory

The fluid flow is expressed by the continuity, momentum and energy equations which describe the conservation of mass, momentum and total energy respectively. Together, they are referred to as the Navier-Stokes equations. These equations are highly nonlinear and fall into the category of second-order partial differential equations, involving four separate variables.

There are two main approaches to describing conservation laws: the Lagrangian approach and the Eulerian approach. In the Lagrangian approach, the fluid is divided into fluid parcels that are tracked as they move through time and space. Each parcel is tagged by a position vector $\vec{x}_0$. The function that describes the movement of the parcel is $\vec{x}(t, \vec{x}_0)$. The Eulerian approach on the other hand focuses on a specific volume element through which the fluid flows over time. The flow variables are therefore a function of the position $\vec{x}$, the time t and the flow velocity $\vec{v}(\vec{x}, t)$. These two equations can be coupled as follows:

$$\vec{v}\left(\vec{x}\left(\vec{x}_0, t\right), t\right) = \frac{\partial}{\partial t}\vec{x}\left(\vec{x}_0, t\right) \tag{2.4}$$

To describe the change of a material volume in the Eulerian specification, Reynolds Transport Theorem is used:

$$\left(\frac{d\phi}{dt}\right)_{MV} = \int_V \left[\frac{\partial}{\partial t}\left(\rho\frac{d\phi}{dm}\right) + \nabla\cdot\left(\rho\vec{v}\frac{d\phi}{dm}\right)\right] dV \tag{2.5}$$

2.1.1 Continuity Equation

The continuity equation states that mass remains constant within a flow. It states that for a given volume, the total mass entering and exiting per unit time must be equivalent to the change in mass caused by density changes over the same period [8]. In the Lagrangian system it is defined as:

$$\left(\frac{dm}{dt}\right)_{MV} = 0 \tag{2.6}$$

Using Equation (2.5) this equation can be converted into the Eulerian system. For a fluid of mass m, density ρ, and velocity $\vec{v}$, this will give:

$$\frac{\partial \rho}{\partial t} + \nabla \cdot [\rho \vec{v}] = 0 \tag{2.7}$$

Alternatively in the integral form for a control volume V:

$$\int_V \left(\frac{\partial \rho}{\partial t} + \nabla \cdot [\rho \vec{v}]\right) dV = 0 \tag{2.8}$$

2.1.2 Momentum Equation

The principle of momentum conservation states that when there are no external forces acting on a body, the total momentum of the body remains constant. Furthermore, as momentum is a vector, its individual directional components will also remain constant. This fundamental concept is defined in Newton's Second Law of Motion [10]. Whena specific volume of material is concerned in the Lagrangian system, it can be expressed in the following form:

$$\left(\frac{d(m\vec{v})}{dt}\right)_{MV} = \left(\int_V \vec{f} dV\right)_{MV} \tag{2.9}$$

Here, $\vec{f}$ is the sum of the external forces acting on the material volume with mass m, density ρ, and velocity $\vec{v}$. Again using (2.5), the conservative form for an Eulerian system can be expressed as:

$$\frac{\partial}{\partial t}[\rho \vec{v}] + \nabla \cdot (\rho \vec{v} \vec{v}) = \vec{f} \tag{2.10}$$

Also in integral form in control volume V:

$$\int_V \left[\frac{\partial}{\partial t}[\rho\vec{v}] + \nabla\cdot(\rho\vec{v}\vec{v}) - \vec{f}\right] dV = 0 \tag{2.11}$$

The external forces $\vec{f}$ include the surface forces $\vec{f_S}$ and the body forces $\vec{f_b}$ as follow:

$$\vec{f} = \overrightarrow{f_S} + \overrightarrow{f_b} \tag{2.12}$$

2.1.3 Energy Equation

The conservation of energy is based on the first law of thermodynamics. It states that the total energy of a closed system remains constant over time, regardless of the processes or interactions occurring within the system. In simpler terms, energy cannot be created or destroyed. It can only be transferred or transformed from one form to another. Therefore the total energy of an isolated system remains constant [5]. The total energy E of a material volume can be expressed as the sum of its internal and kinetic energies:

$$E = m\left(\epsilon + \frac{1}{2}\vec{v}\cdot\vec{v}\right) \tag{2.13}$$

Here m is the mass and ε is the specific internal energy of the fluid. The total energy of a material volume changes only through the heat flow $\dot{Q}$ and performed work $\dot{W}$.

$$\left(\frac{dE}{dt}\right)_{MV} = \dot{Q} - \dot{W} \tag{2.14}$$

The heat flow can be divided into two components: the flow across the surfaces, denoted as $\dot{Q}_S$, and the heat generated or consumed inside the volume, denoted as $\dot{Q}_V$. Also the work can be split into the work performed by the surface forces $\dot{W}_S$ and work performed by the body forces $\dot{W}_b$. Using these equations, one can express the conservation of energy in terms of the specific total energy $e = \frac{E}{m}$ as:

$$\frac{\partial}{\partial t}(\rho e) + \nabla\cdot[\rho\vec{v}e] = -\nabla\cdot\dot{q}_S - \nabla\cdot[p\vec{v}] + \nabla\cdot[\overline{\overline{\tau}}\cdot\vec{v}] + \rho\vec{g}\cdot\vec{v} + \dot{q}_V \tag{2.15}$$

The equation can also be expressed in its integral form for a control volume V:

$$\int_V \left(\frac{\partial}{\partial t}(\rho e) + \nabla \cdot [\rho \vec{v} e] + \nabla \cdot \dot{q}_S + \nabla \cdot [p \vec{v}] - \nabla \cdot [\bar{\bar{\tau}} \cdot \vec{v}] - \rho \vec{g} \cdot \vec{v} - \dot{q}_V \right) dV = 0 \tag{2.16}$$

2.1.4 Navier-Stokes Equation

The Navier-Stokes equations are partial differential equations that describe and predict the behavior of fluid flow under various conditions by applying conservation principles. The equations are derived from the basic principles of conservation of mass and Newton's second law of motion. These equations are typically written in vector form and expressed in terms of the fluid's velocity, pressure, density, and viscosity. They are applicable to three-dimensional flows [30].

$$\nabla \cdot \vec{V} = 0 \tag{2.17}$$

$$\rho \left(\frac{\partial \vec{V}}{\partial t} + \vec{V} \cdot \nabla \vec{V} \right) = -\nabla p + \mu \nabla^2 \vec{V} + \vec{S} \tag{2.18}$$

Where $\vec{V}$ is the velocity vector, t is time, ρ is density, p is the pressure, μ is the viscosity, $\vec{S}$ is a source term, and ∇^2 is the Laplacian operator.

2.2 Computational Fluid Dynamics

CFD is a method used to numerically simulate fluid flow and heat transfer processes. Mathematical models and numerical methods are employed to resolve, gather data, and analyze problems related to fluid flows. It's particularly useful in engineering where it may be difficult or impractical to perform physical experiments. CFD utilizes numerical methods to solve fluid flow problems, specifically the Navier-Stokes (N-S) equations. These equations can be presented either in a compact form for incompressible flows or in a Cartesian form. These equations describe the motion of any Newtonian fluid.

$$\frac{\partial u}{\partial x} + \frac{\partial v}{\partial y} + \frac{\partial w}{\partial z} = 0 \tag{2.19}$$

$$\rho\left(\frac{\partial u}{\partial t}+u\frac{\partial u}{\partial x}+v\frac{\partial u}{\partial y}+w\frac{\partial u}{\partial z}\right)=-\frac{\partial p}{\partial x}+\mu\left(\frac{\partial^2 u}{\partial x^2}+\frac{\partial^2 u}{\partial y^2}+\frac{\partial^2 u}{\partial z^2}\right)+S_x \tag{2.20}$$

$$\rho\left(\frac{\partial v}{\partial t}+u\frac{\partial v}{\partial x}+v\frac{\partial v}{\partial y}+w\frac{\partial v}{\partial z}\right)=-\frac{\partial p}{\partial y}+\mu\left(\frac{\partial^2 v}{\partial x^2}+\frac{\partial^2 v}{\partial y^2}+\frac{\partial^2 v}{\partial z^2}\right)+S_y \tag{2.21}$$

$$\rho\left(\frac{\partial w}{\partial t}+u\frac{\partial w}{\partial x}+v\frac{\partial w}{\partial y}+w\frac{\partial w}{\partial z}\right)=-\frac{\partial p}{\partial z}+\mu\left(\frac{\partial^2 w}{\partial x^2}+\frac{\partial^2 w}{\partial y^2}+\frac{\partial^2 w}{\partial z^2}\right)+S_z \tag{2.22}$$

Here x, y, z is the Cartesian coordinate system, u, v, w is the Cartesian velocity system, t is time, ρ is density, p is the pressure, μ is the viscosity, and $S_{x,y,z}$ is the source term.

The Navier-Stokes equations are challenging to solve directly because they are nonlinear, particularly the convective acceleration terms. There are different turbulence models that can be used to estimate these equations.

2.3 Turbulence Models

Turbulence models are mathematical formulas used in CFD to simulate the behavior of turbulent flows. Turbulence refers to the chaotic and irregular motion of fluid particles within a flow field. It is characterized by variations in velocity, pressure, and other flow properties at different scales.

There are several types of turbulence models, such as Reynolds-Averaged Navier-Stokes (RANS) models, Large Eddy Simulation (LES), and Direct Numerical Simulation (DNS). The selection of a model depends on various factors, including the nature of the flow, the available computational resources, and the desired level of accuracy.

2.3.1 Large Eddy Simulations

Large Eddy Simulation (LES) is a computational method that aims to capture the dominant turbulent structures in a flow while also accounting for the influence of smaller scales. This is achieved by applying a spatial filter to the governing Navier-Stokes equations. The filter segregates the flow into larger-scale resolved structures and smaller-scale modeled structures.

LES is ideal for simulating complex and unsteady turbulent flows, where accurately representing large-scale structures is important. It's often used in scenarios like combustion processes and aerodynamic simulations around vehicles and buildings.

Due to its high computational demands, LES is typically performed on high-performance computing platforms. It requires substantial memory and processing capabilities, which can limit its applicability in some cases.

2.3.2 Direct Numerical Simulations

Direct Numerical Simulation (DNS) is a CFD technique used to simulate fluid flows with the highest level of detail. DNS aims to resolve all scales of turbulent motion, from the largest to the smallest.

DNS is mainly applied to flows where turbulence plays a dominant role and the details of the turbulent structures are of main interest. It's commonly used in studies of boundary layers, wakes, and simple geometries.

DNS is computationally very expensive, and it requires significant computing resources. It demands a fine grid resolution, which leads to a large number of grid points. As a result, DNS is typically limited to relatively simple geometries and low Reynolds number flows.

2.3.3 Reynolds-Averaged Navier-Stokes Simulations

Reynolds-Averaged Navier-Stokes (RANS) simulations are based on time-averaged equations of motion. Which means that the flow variables are decomposed into their time-averaged and fluctuating components. The equations are then solved for the mean flow properties.

RANS simulations assume that turbulence is steady and can't capture unsteady or transient flow behavior. Additionally, they may struggle with accurately predicting flow separation, complex three-dimensional flows, and flows with significant swirling or vortex-dominated structures. The effects of turbulence on the flow are modeled using turbulence models. These provide additional equations to close the system of equations.

k-epsilon Turbulence Model

The k-epsilon turbulence model is a widely used two-equation model to simulate flow characteristics for turbulent flow conditions. The k-epsilon model solves for two transport equations: turbulent kinetic energy (k) and its dissipation rate (epsilon). It states that turbulence can be described by a turbulent viscosity, which is related to the turbulent kinetic energy and assumes that the turbulence is isotropic, which means that the turbulence properties are the considered to be the same in all directions [1].

The standard k-epsilon model is generally used for simulations since the generalized k-epsilon model contains many unknowns and unmeasurable terms. It is based on the equations below:

$$\text{Continuity Equation } = \frac{\partial \rho}{\partial t} + \nabla \cdot (\rho \mathbf{u}) = 0 \tag{2.23}$$

$$\text{Navier-Stokes Equation} = \rho \left(\frac{\partial \mathbf{u}}{\partial t} + \mathbf{u} \cdot \nabla \mathbf{u} \right) = -\nabla p + \mu \nabla^2 \mathbf{u} \tag{2.24}$$

$$\text{Turbulent Kinetic Energy Equation} = \frac{\partial(\rho k)}{\partial t} + \frac{\partial(\rho k u_i)}{\partial x_i} = \frac{\partial}{\partial x_j}\left[\frac{\mu_t}{\sigma_k}\frac{\partial k}{\partial x_j}\right] + 2\mu_t E_{ij} E_{ij} - \rho\varepsilon \tag{2.25}$$

$$\text{Turbulent Dissipation Rate} = \frac{\partial(\rho\varepsilon)}{\partial t} + \frac{\partial(\rho\varepsilon u_i)}{\partial x_i} = \frac{\partial}{\partial x_j}\left[\frac{\mu_t}{\sigma_e}\frac{\partial \varepsilon}{\partial x_j}\right] + C_{1\varepsilon}\frac{\varepsilon}{k} 2\mu_t E_{ij} E_{ij} - C_{2\varepsilon}\rho\frac{\varepsilon^2}{k} \tag{2.26}$$

The k-epsilon turbulence model has earned a good reputation in the field of simulations, having several advantages and drawbacks. Regarding it‘s advantages, it is known for its robustness and extensive application, even in presence of acknowledged limitations. It‘s ease of implementation and computational efficiency further enhance its appeal. It‘s particularly useful in scenarios characterized by fully turbulent flows, making it a fitting choice for initial iterations, first assessments of alternative designs investigations. However, the model does exhibit notable weaknesses. It tends to struggle in handling complex flows that have severe pressure gradients, separation phenomena, or sharp changes in streamline curvature. One of it's most significant drawbacks is the limited sensitivity to adverse pressure gradients, which can lead to inaccuracies in certain situations. Additionally, the model may encounter numerical stiffness issues when solving it's equations, presenting an additional challenge to it's applications [15].

k-omega-SST Turbulence Model

The k-omega SST turbulence model is a two-equation eddy-viscosity hybrid model that combines aspects of both the k-epsilon and k-omega models. It uses a blending function to transition between the two models based on the local flow conditions. The use of a k-ω formulation in the inner parts of the boundary layer makes the model directly usable all the way down to the wall through the viscous sub-layer. The SST formulation also switches to a k-ε behaviour in the free-stream and thereby avoids the common k-ω problem that the model is too sensitive to the inlet free-stream turbulence properties. It is based on the equations below:

$$\text{Turbulent Dissipation} = \nabla\cdot(\rho D_\omega \nabla\omega) + \frac{\rho\gamma G}{\nu} - \frac{2}{3}\rho\gamma\omega(\nabla\cdot\mathbf{u}) - \rho\beta\omega^2 - \rho\left(F_1 - 1\right)CD_{k\omega} + S_\omega \tag{2.27}$$

$$\text{Turbulent Kinetic Energy} = \nabla\cdot(\rho D_k \nabla k) + \rho G - \frac{2}{3}\rho k(\nabla\cdot\mathbf{u}) - \rho\beta^*\omega k + S_k \tag{2.28}$$

This model achieves a wide range of accuracy across various flow conditions, striking a balance between precision and computational efficiency. The SST turbulence model exhibits excellent performance in critical areas like near-wall regions, adverse pressure gradients, and intricate flow patterns. However, its dependence on wall distance makes it less adept for free shear flows compared to the standard k-w model, requiring a higher mesh resolution near the wall [17].

3 Modeling

The relatively simple receiver models were created using CATIA V5. The analysis of the cavity's flow was performed by simulating it using ANSYS CFX (Version 2023 R1). The model configuration covers defining the receiver's geometry and domain, generating the computational mesh, and establishing the model's boundary conditions. As explained the new receiver design is constructed as an open cavity with an inner square-cone shape. To determine the ideal design of the receiver it was examined for different aperture depth variations from 50 mm to 200 mm. These distinct receivers were created in CATIA V5 environment. All receiver designs have an aperture length of 200 mm, while the length of the top side is defined to be 140 mm.

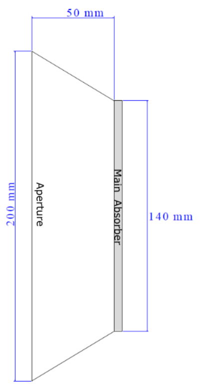

(a) Receiver design with 50 mm depth

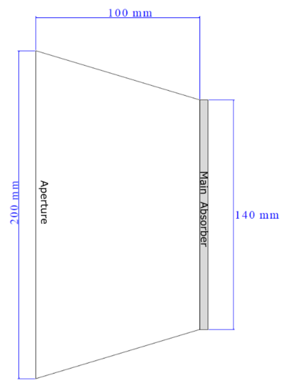

(b) Receiver design with 100 mm depth

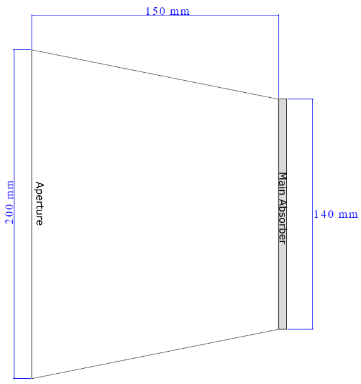

(c) Receiver design with 150 mm depth

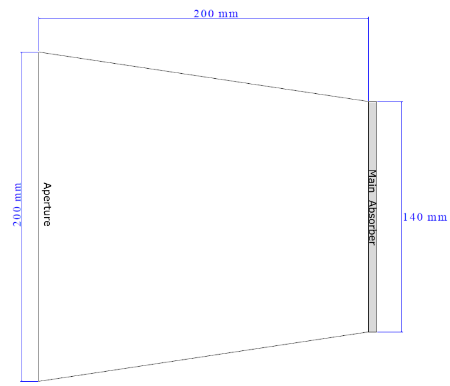

(d) Receiver design with 200 mm depth

Figure 10: Receiver design variations

The main absorber is a wire mesh absorber with a 5 mm thickness and has a porous structure. It utilizes a volume porosity of 0.5. The defined volume porosity of the material is a measure of the void space in the material. The higher the porosity, the more void space there is in the material. This porous surface promises efficient solar energy capture and conversion. The porous absorber in cavity receivers serves to enhance heat transfer and reduce thermal losses. It does this by increasing the surface area available for absorbing and transferring heat from the incoming air or heat transfer medium. This means that more thermal energy can be efficiently absorbed, leading to higher temperatures within the cavity. Additionally, the porous nature of the absorber allows for better airflow and circulation, which helps distribute heat more effectively. This can lead to more uniform temperatures and reduce the risk of overheating in localized areas [23].

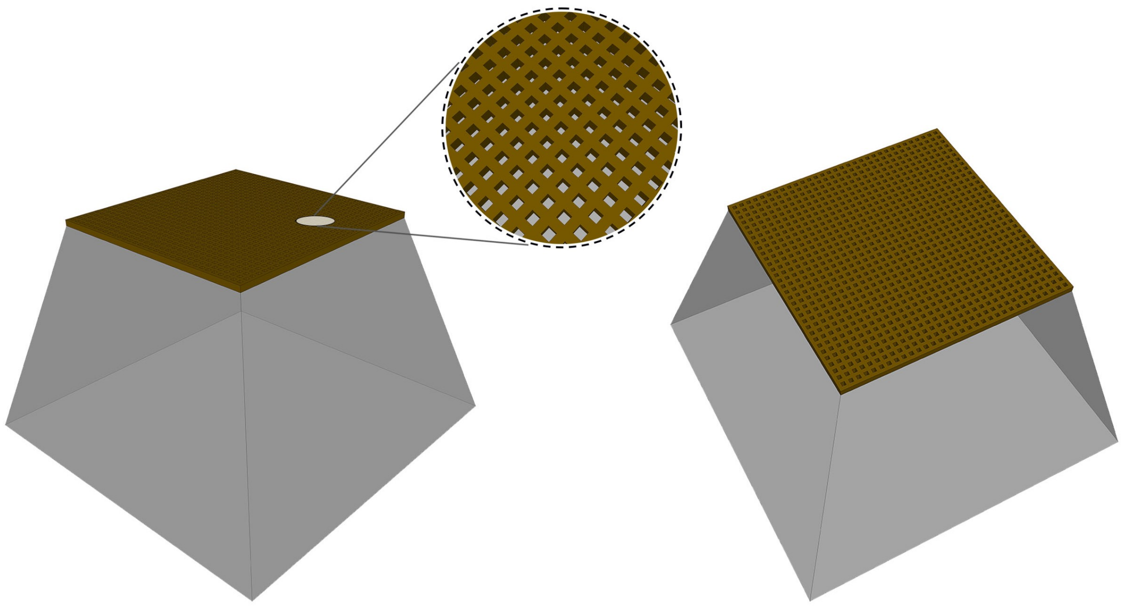

Figure 11: Porous main absorber for the new concept receiver (wire mesh region for inlet absorber not shown)

The temperature profiles within these receivers will differ depending on their individual depths. Figure 12 displays the four distinct configurations arranged together.

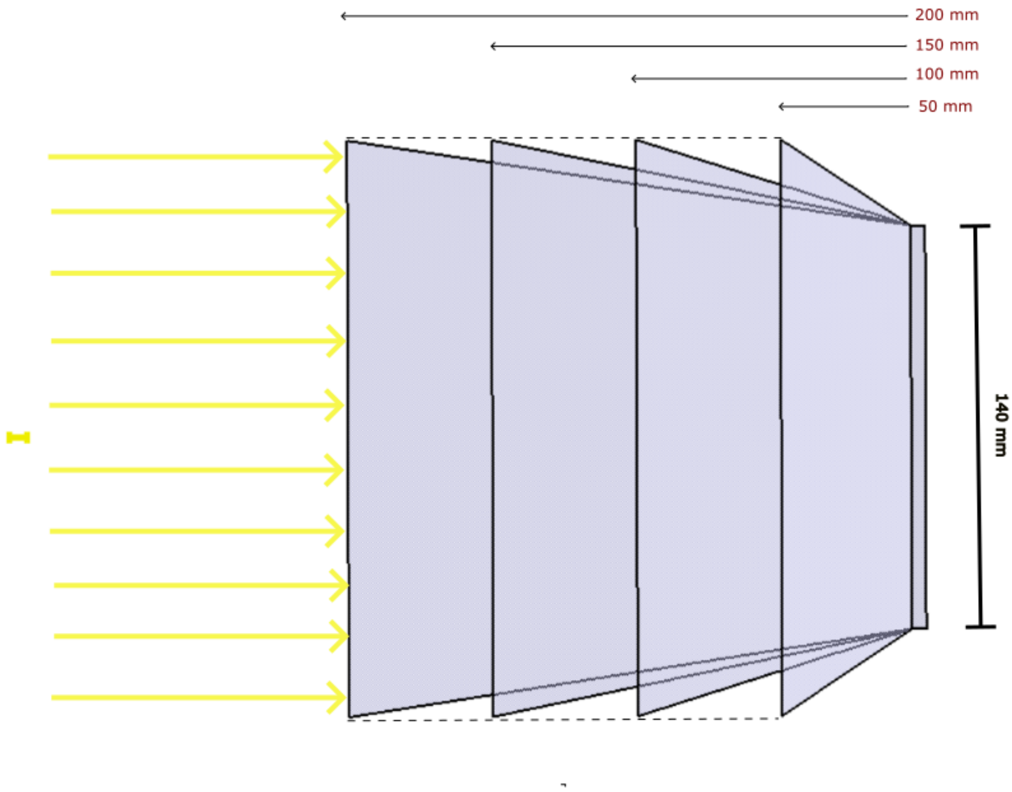

Figure 12: Receiver variations arranged together

$$I_{50\ \mathrm{mm}} = I_{100\ \mathrm{mm}} = I_{150\ \mathrm{mm}} = I_{200\ \mathrm{mm}} \tag{3.29}$$

The incoming radiation is constant across all variations (Equation 3.29). Assuming uniform aperture lengths and constant incoming irradiation across all variations, the aperture depth will be the main distinguishing factor. The incoming radiation refers to the electromagnetic energy that is received by a surface or object from its surroundings. In the context of a solar receiver, incoming radiation primarily originates from the Sun. It is expected that the temperature distribution will be the primary distinguishing factor. The receiver with the lowest receiver depth is likely to achieve higher surface temperatures. This is because the concentrated incoming radiation is spread over a smaller volume (Equation 3.30), resulting in more intense heating. It may also mean that the thermal gradient within the receiver is steeper, potentially leading to higher peak temperatures and increased thermal stresses.

$$\frac{I_{50\ \text{mm}}}{\text{Volume}_{\ 50\ \text{mm}}} \neq \frac{I_{100\ \text{mm}}}{\text{Volume}_{\ 100\ \text{mm}}} \neq \frac{I_{150\ \text{mm}}}{\text{Volume}_{\ 150\ \text{mm}}} \neq \frac{I_{200\ \text{mm}}}{\text{Volume}_{\ 200\ \text{mm}}} \tag{3.30}$$

The receiver with a moderate depth strikes a balance between surface temperature and thermal distribution. It would attain more evenly distributed surface temperatures due to the concentrated incoming radiation, potentially resulting in a more uniform temperature profile.

The receiver with the greatest aperture depth may have lower surface temperatures when compared to receivers with shallower depths. This is because the incoming radiation is dispersed over a larger area, resulting in less intense heating at the surface. However, the greater depth enables improved absorption and distribution of heat within the material, potentially resulting in a more consistent and even temperature distribution.

Briefly, while all receivers have the same aperture lengths and incoming radiation, their varying depths will influence the temperature distribution and peak temperatures. The selection of receiver depth should be carefully evaluated, considering factors such as material properties, thermal stress, and desired temperature profiles for the specific application.

3.1 Computational Domain

After designing the receiver model, a negative is created that represents the air-filled receiver opening also described as the computational space for the ambient. When determining the appropriate size of the computational domain for external aerodynamics problems, having prior knowledge of the body's impact on the surrounding flow field can be advantageous. This can be achieved by analyzing previous CFD simulations with similar geometries or by conducting a simulation with an oversized domain. However, when such data is unavailable like in this case or when a large domain is computationally not practical, experienced-based estimation and best practices can be used to approximate the domain dimensions. A large enough space should be allowed around the geometry of interest. If the distance is too small, the numerical boundary conditions can lead to non-physical effects on the flow field as the algorithm forces the flow to adhere to the boundary conditions. Upstream of the body, a recommended starting point is to have a minimum domain length of roughly twice the body's length. This provides enough space for the flow to adjust to the presence of the geometry. Downstream, the body typically generates a wake of lower energy flow, convected by the main flow. Therefore, it is advisable to have a domain length of at least five times the body's dimension along the direction of the flow to accommodate the boundary condition imposed at the domain outlet. Similarly, leaving approximately twice the body's width on each side allows for local flow deviations [4].

Figure 13: Air Filled Receiver Opening

Figure 13, displays the computational space, depicted by the transparent sections, where the ambient air interacts with the receiver's aperture. For the simulation, this space was modeled as a rectangular prism. As per recommendations, its dimensions were selected to be approximately five times larger than those of the simulated model.

3.2 Discretization

3.2.1 Mesh Requirements

The accuracy of the results obtained by performing the required simulations is highly dependent on the quality of the generated grids. A poor quality grid can lead to instability and poor accuracy [19]. Care should always be taken to create high-quality meshes by maintaining the balance between quality and computational time, as high-quality meshes can often lead to high computing times.

The grid should ideally be free of gaps or elements that are overlapping. Additionally, it's important to concentrate grid points around points of interest, such as locations with significant gradients like boundary layers, separation points, and shocks. Regions where pressure changes are anticipated, as well as around sharp corners or curves. There are various ways to analyze the quality of the generated mesh. One can control some parameters like the aspect ratio, skewness and orthogonal quality for that purpose.

3.2.2 Mesh Method

In the simulations for the first and second part of the analyses two distinct approaches were employed. Approach one will be used to point out the best geometry variance with regards to the ARR and approach two will be used to determine the dependencies of the ARR on the mass flow gradient and temperature gradient on the receiver. The most significant distinction between these two approaches lies in the treatment of the receiver. In approach one, the receiver geometry is modified as a single entity. Conversely, in approach two, the receiver geometry is divided into five segments, which will later be utilized to integrate the distributions of mass flow and temperature gradient.

3.2.3 Approach One

In order to ensure comprehensive analysis of the entire domain and the receiver, a comprehensive methodology known as "approach one" was implemented. This approach allows for a thorough examination of the flow dynamics and heat transfer characteristics. As depicted in the figures, the mesh refinement is particularly concentrated towards the edges of the receiver. This strategic refinement significantly enhances the resolution, facilitating a more precise analysis of buoyancy effects and boundary conditions. By employing this methodology, the aim is to achieve a comprehensive understanding of the flow behavior within the receiver's cavity, ultimately aiding in the selection of the optimal geometry.

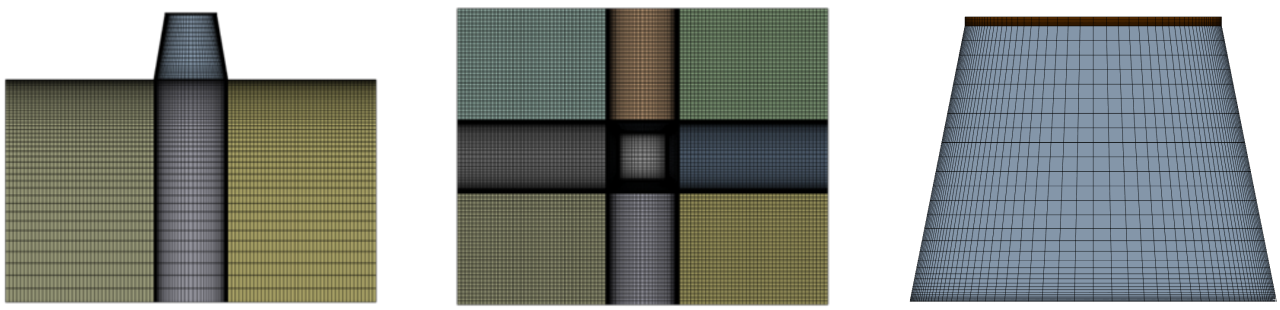

(a) Front View **(b)** Top View **(c)** Absorber

Figure 14: Meshing for Approach One

3.2.4 Approach Two

Approach two involves partitioning the absorber's layout into five separate segments. This division enables the incorporation of different mass flow and temperature gradients, which will play a crucial role in determining their respective ARR in subsequent calculations. To increase the accuracy of the results, the mesh is tailored to be finer at the interfaces between these segments, with increased density towards the edges. This methodology mirrors a technique utilized in approach one, affirming a comprehensive and precise analysis.

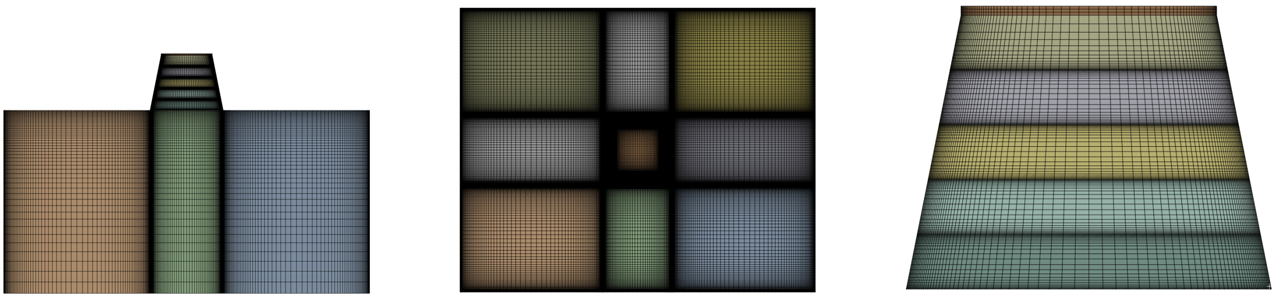

(a) Front View **(b)** Top View **(c)** Absorber

Figure 15: Meshing for Approach Two

3.2.5 Mesh Type

To ensure precise CFD simulations, generating a high-quality mesh is crucial. In this section, special emphasis is placed on the cavity. The computational grids used consist of structured meshes and were created with ANSYS. A bias factor is established to achieve a finer discretization near the edges, allowing for a more detailed observation of the buoyancy effects and inflow-outflow effects, while also considering the trade-off between accuracy and computational time.

Meshes are commonly categorized into two primary types: structured and unstructured. Structured meshes exhibit an inherent connectivity pattern that facilitates the straightforward identification of elements and nodes. This type of mesh frequently employs orthogonal quadrilateral elements in two dimensions and hexahedral elements in three dimensions, as demonstrated in Figure 16.

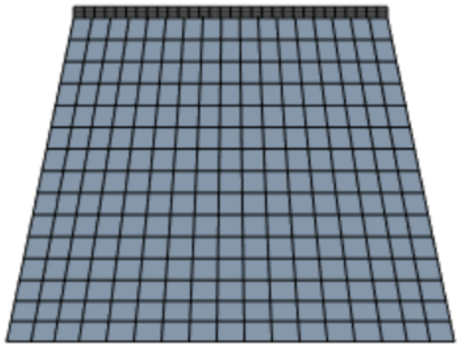

Figure 16: Structured Mesh

Structured meshes lend themselves to efficient data management and processing. Nodes can be analyzed in a systematic manner, enabling easy calculation between neighboring elements or nodes without the need for extensive connectivity information. This characteristic streamlines computational tasks and facilitates the implementation of algorithms that rely on proximity-based operations. Furthermore, the consistent element size across the mesh ensures straightforward access to coordinates, simplifying calculations and operations that require precise spatial information. This uniformity in element size is particularly advantageous when performing numerical computations and simulations, contributing to the overall efficiency of the analysis.

On the contrary, unstructured meshes do not stick to a predetermined, organized connectivity pattern. Instead, they offer greater flexibility in representing complex geometries and irregular shapes. These meshes comprise various element types, employing triangles in two-dimensional simulations and tetrahedrals in 3D scenarios. While structured meshes excel in simplicity and ease of element and node identification, unstructured meshes prove invaluable in tackling complex and irregular geometries that do not neatly align with a structured grid. This adaptability is crucial for accurately simulating real-world scenarios characterized by complex shapes and variable boundary conditions.

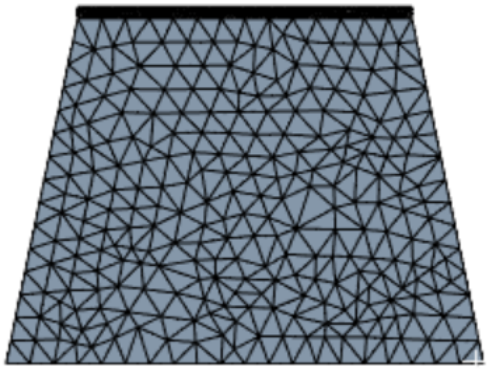

Figure 17: Unstructured Mesh

However, the discretization was executed with the use of structured meshes which offer several advantages in contrast to unstructured meshes:

- Structured meshes consist of well-organized grids with a regular pattern which are easy to apply to relatively simple and regular geometries.
- Structured meshes can be highly efficient and accurate, particularly when dealing with geometries that align well with grid lines including improved resolution and a higher convergence rate.
- The regularity can lead to better representation of flow and heat transfer phenomena.
- Structured meshes excel at accurately representing boundary layers, a vital aspect in heat transfer calculations near surfaces.

3.3 Mesh Independent Study

This thesis highlights the importance of the ARR in its findings. To ensure the accuracy of the results, a mesh independence study will be performed by using four different computational grids with varying levels of fineness. This analysis will focus on the receiver with the depth of 150 mm. These grids, which consist of structured mesh elements, were generated using ANSYS (Version 2023 R1). Since two different mesh strategies were used in the analysis, a mesh independence study was conducted for each one. The ARR values obtained, along with the corresponding element counts for each computational grid, are provided in both Table 1 and Table 2.

Table 1: Mesh Independent Study for Approach One

Mesh	**Number of Elements**	**ARR** [%]]
Coarse	0.40 Mill	95.02
Middle	0.82 Mill	94.48
Fine	1.15 Mill	94.53
Very Fine	1.60 Mill	94.53

Table 2: Mesh Independent Study for Approach Two

Mesh	**Number of Elements**	**ARR** [%]
Coarse	1.12 Mill	94.87
Middle	1.14 Mill	94.47
Fine	1.67 Mill	94.42

The variation in the ARR among the distinct computational grids can be calculated as 0.002 percentage points for the first approach and 0.005 percentage points for the second approach. Notably, in the first approach, it is clear that the ARR has a greater degree of stability as the level of fineness increases, with fluctuations nearly diminishing between the fine and very fine meshes. Consequently, the fine mesh, consisting of 1.1 million elements, was selected for further investigations within further investigations of the first approach. For approach two the ARR doesn't shows not noticeable change dependent on the number elements after the middle mesh. Therefore the middle mesh was chosen to prevent unnecessary computational time.

3.4 Mesh Quality

The quality of the mesh is another critical factor in finite element applications, as it directly affects the efficiency and accuracy of the simulation. It is universally recognized that the precision and computational effectiveness of finite element solutions depend on the dimensions and configuration of the elements, which are, in turn, shaped by the quality of the underlying mesh. To get a better understanding of mesh quality, analysis on the aspect ratio, orthogonal quality and skewness of the mesh have to be made [28].

Aspect Ratio

The aspect ratio is the ratio of a cell's longest length to the shortest length. A high aspect ratio means that one edge is significantly longer than the others. This can result in distorted elements. In CFD simulations, elements that have extremely high aspect ratios can result in numerical instability and inaccuracies in the obtained results. The optimal aspect ratio value is 1. The formulation of the aspect ratio is as follows:

$$\text{Aspect Ratio } = \frac{\max\left(x_1, x_2, \ldots, x_{12}\right)}{\min\left(x_1, x_2, \ldots, x_{12}\right)} \tag{3.31}$$

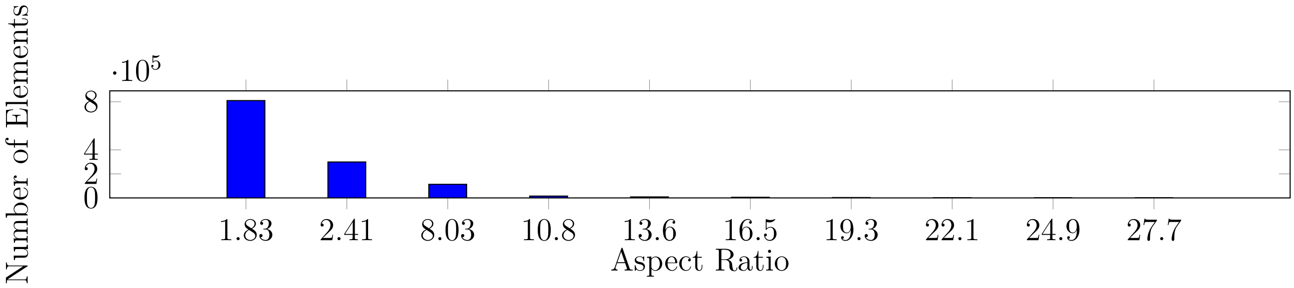

Figure 18: Aspect Ratio for Approach One

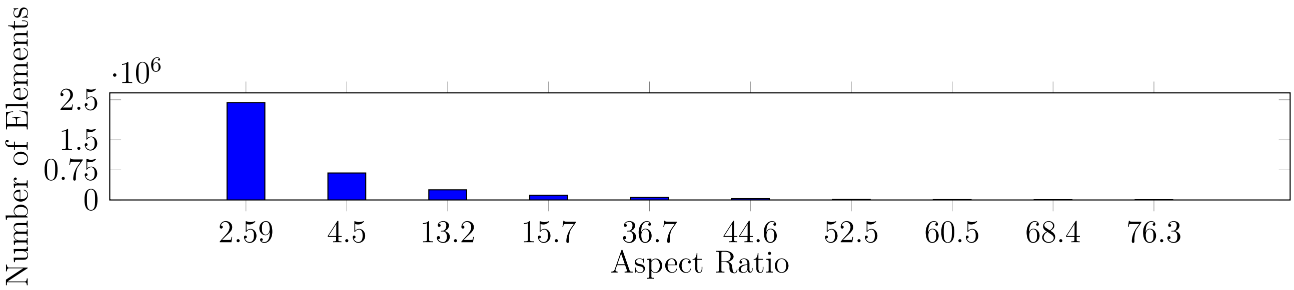

Figure 19: Aspect Ratio for Approach Two

From the aspect ratio investigations obtained from ANSYS for approach one and approach two it can be stated that the created mesh has a high quality aspect ratio distribution, which promises results that have a high probability of convergence and accuracy for the simulations.

Skewness

Skewness refers to the deviation between the optimal cell size and the actual cell size within a mesh. The skewness value falls between 0 (ideal) and 1 (worst). Elements with high skewness are undesirable as they can lead to reduced accuracy in interpolated regions. The method for calculating skewness varies depending on the type of cell being used:

$$Skewness = \max\left(\frac{\theta_{\max} - 90}{180 - 90}, \frac{90 - \theta_{\min}}{90}\right) \tag{3.32}$$

Inspecting the skewness of the generated mesh it can be seen that the overall values are nearly zero, which can be interpreted as excellent.

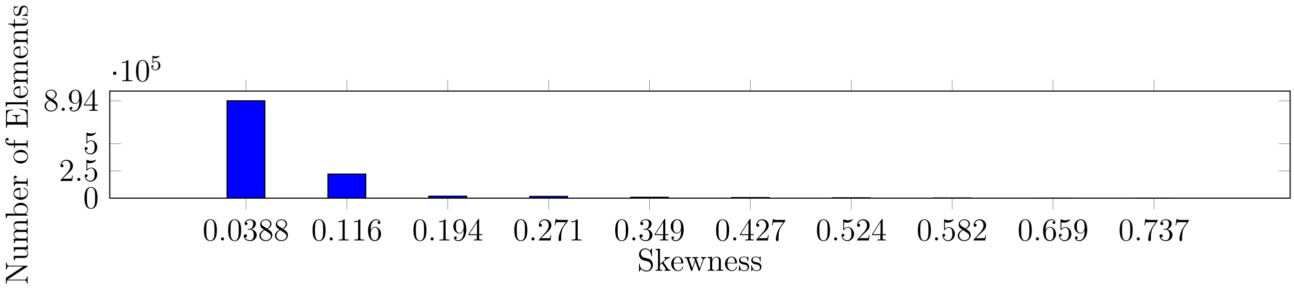

Figure 20: Skewness for Approach One

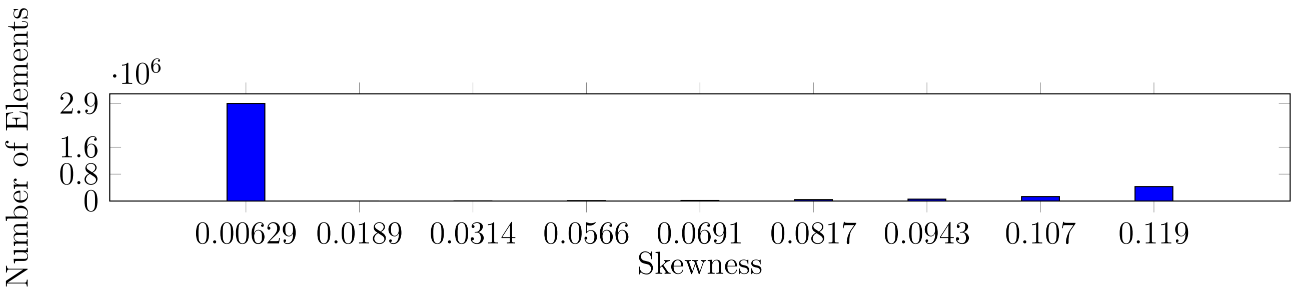

Figure 21: Skewness for Approach Two

Orthogonal Quality

Orthogonal quality refers to the degree to which the grid lines or edges of mesh elements (such as triangles, quadrilaterals, tetrahedra, etc.) are perpendicular or orthogonal to each other at their intersection points. A grid with high orthogonality will have grid lines that intersect at close to 90-degree angles, while a grid with low orthogonality will have grid lines that intersect at acute angles. The range for orthogonal quality is from 0 to 1. A value of 0 represents the worst quality, while a value of 1 represents the best quality.

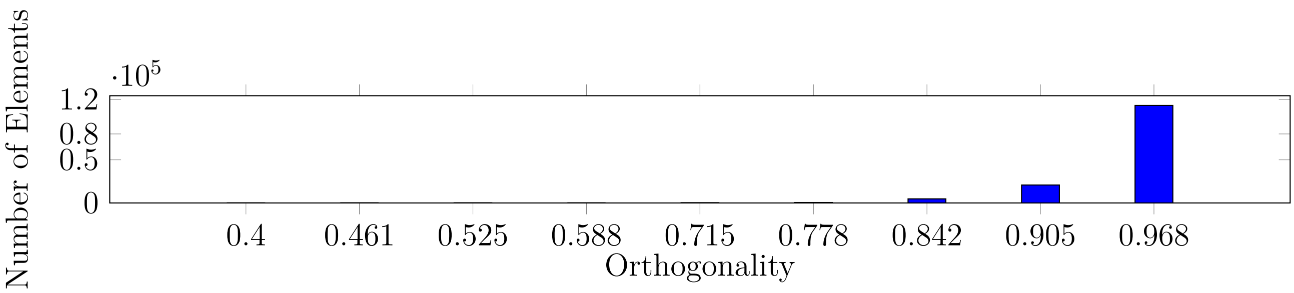

Figure 22: Orthogonality for Approach One

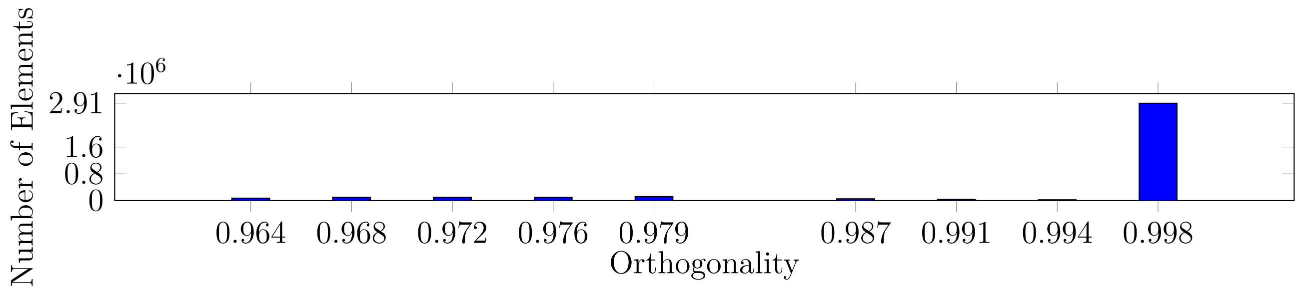

Figure 23: Orthogonality for Approach Two

3.5 CFD Solver Process

The computer-generated model allows engineers to test various design parameters and scenarios quickly through iterations and simulations. This significantly shortens the time required for testing. This testing process not only speeds up the development cycle but also results in a more efficient final design. It's important to note that the computer-generated model may not capture every detail of the real-world counterpart, it serves as an effective tool for refining fluid dynamics within the virtual atmosphere. This convergence of digital analysis and physical reality is a testament to the remarkable capabilities of modern engineering techniques.

3.5.1 Simulation Software

The examination of the reference absorber was conducted through flow simulations utilizing the CFD software ANSYS CFX (2023 R1). Developed by Ansys Inc., ANSYS CFX is known for its advanced proficiency in replicating complex fluid flow and heat transfer phenomena. The software employs the finite volume method to dissect the governing equations, leading to accurate forecasts of flow characteristics, turbulence patterns, and heat transfer dynamics. Additionally, CFX offers simulation of multiphase systems.

ANSYS CFX's extensive range of turbulence models and heat transfer options enhances its adaptability in handling a broad range of scenarios. This allows engineers and researchers to select the most appropriate models for their specific applications, ensuring accurate and reliable results. The software's ability to handle complex geometries further expands its applicability, making it an indispensable tool for engineers and researchers grappling with intricate fluid flow and heat transfer challenges.

3.5.2 CFD - Model Setup

The analysis will employ the pressure-based approach, as the analysis are dealing with low-speed, incompressible airflow for the receiver. Once the approach is chosen, it's essential to specify the fluid properties, which may involve parameters like viscosity and density.

In the setup interface correctly defining the boundary conditions is one of the most crucial aspects of setting up the model to ensure precise results later on. The residual monitors, generated during the analysis solving process, are highly beneficial and are set to low values for high accuracy results. For a straightforward geometry like the the , a residual value of 10^-5 would be sufficient for initial simulations. In Figure 24, the diagram of the workflow is depicted for better understanding of the entire workflow of the CFD analysis.

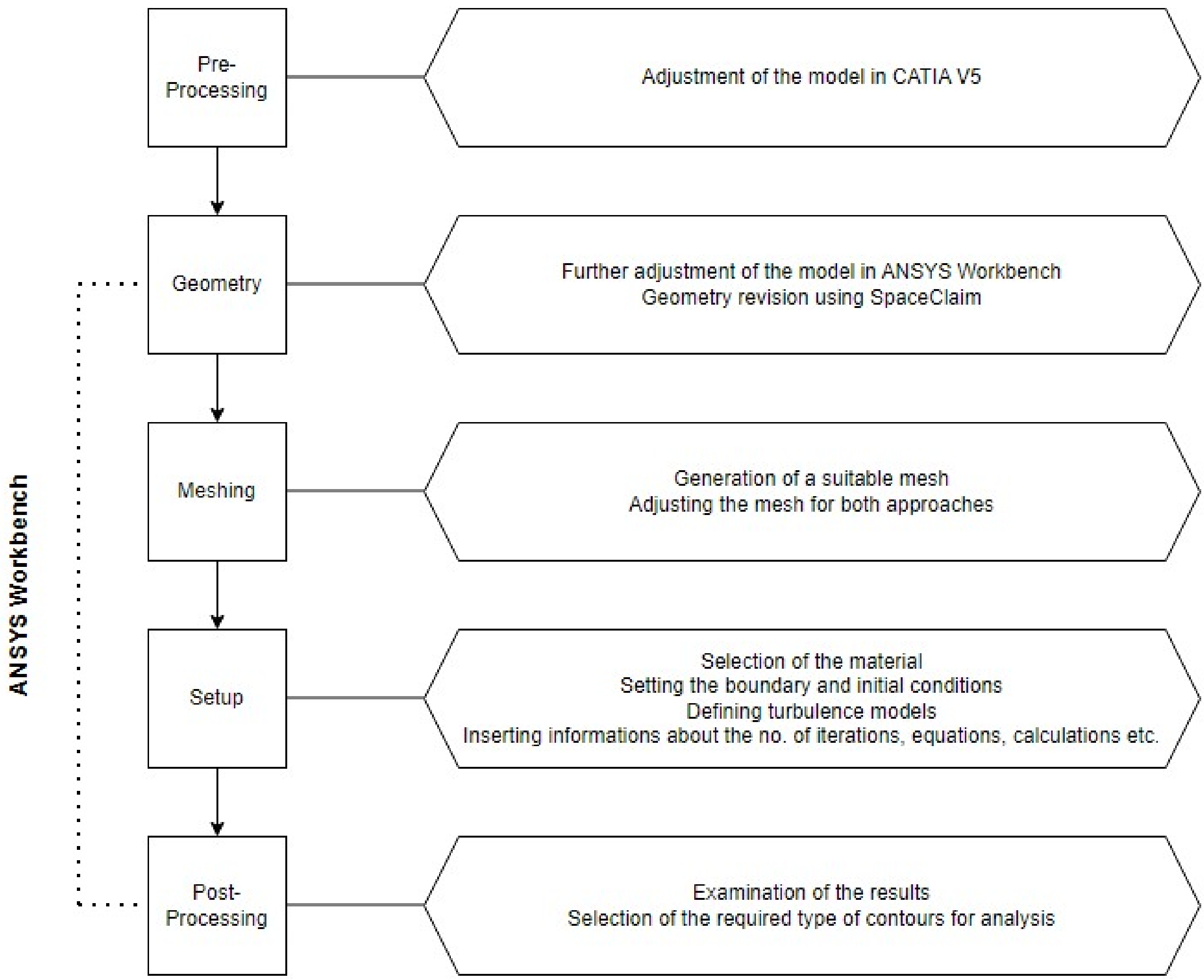

Figure 24: Workflow diagram of the CFD analysis

3.5.3 Boundary Conditions

Careful consideration of boundary conditions ensures that the CFD model accurately represents the real-world physical environment being simulated. This step is crucial for obtaining reliable results because any inaccuracies in boundary conditions can cause significant discrepancies between the simulated and actual model. Engineers establish parameters such as inflow velocities, temperatures, and pressure gradients in order to replicate the dynamic conditions of the system being studied. Additionally, accurate representation of solid boundaries and their thermal properties is crucial for capturing heat transfer phenomena. The careful attention given to setting these boundary conditions demonstrates a dedication to creating simulations that not only match theoretical expectations but also accurately represent the complexities of the real world. This careful approach ultimately improves the credibility and usefulness of the CFD analysis in guiding engineering decisions and optimizations.

The model consists of two regions: a fluid domain and a porous domain. The fluid domain represents the channel where the fluid flows, and the porous domain represents the porous effects of the main absorber. The fluid domain includes boundaries such as the inlet, ambient, and wall. The negative part on Figure 13, represents the air-filled receiver opening, which can also be called the ambient. The ambient domain must be large enough to capture the boundary effects and it has the shape of a rectangular prism. The only medium defined is air in ideal state. However, a distinction is made between inlet air and ambient air, i.e., air flowing out of the absorber and air from the environment. Therefore, a multi-phase simulation has been carried out. The inlet is defined as the areas of the receiver where the air flows in.

The porous effects are calculated using the porous domain of the main absorber. The porosity is defined based on fabric data, which varies depending on the material used. In general, the setup of the boundary conditions for the model are as follows:

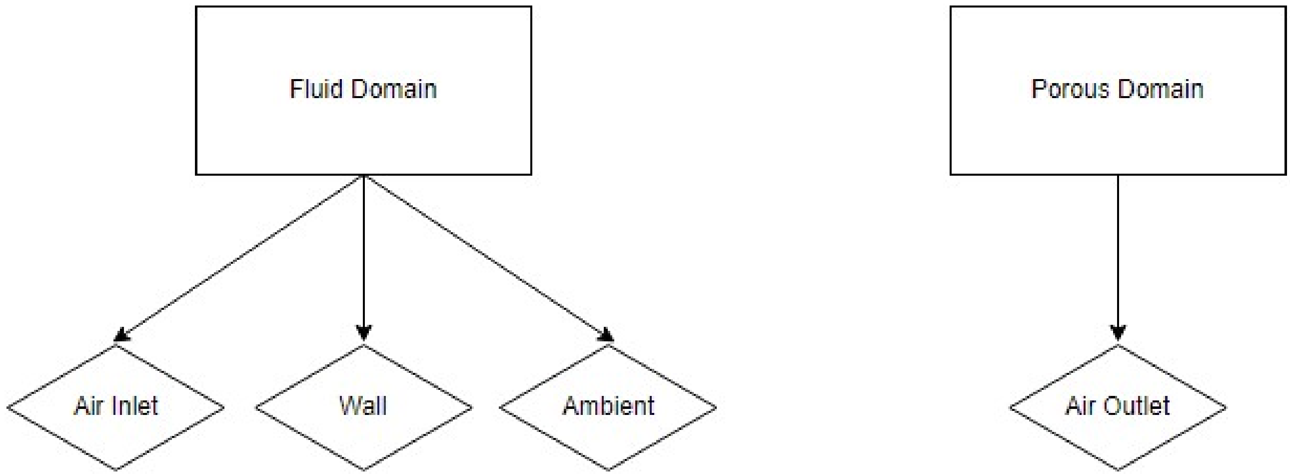

Figure 25: Diagram of boundary conditions

Following information's regarding the build up of the boundary conditions for the previously discussed approach one and approach two will be explained, which includes the illustration of the boundary conditions and their respective configurations.

3.5.4 Fluid Domain

This closed cavity allows for a complete representation of the fluid's behavior within the defined computational domain. It ensures that the way the fluid interacts with its surroundings is accurately captured, which is a crucial aspect in understanding complex fluid flow patterns. Moreover, the non-manifold nature of the region emphasizes the constant connectivity of all points within it. This characteristic is essential for maintaining the integrity of the fluid domain and ensuring accurate computation of flow dynamics. The careful and thorough definition of these terms highlights the precision and exactness of computational fluid dynamics. This provides a strong foundation for simulations that are both robust and reliable.

Table 3: Fluid Domain Boundary Configurations

Type	Fluid Domain
Material Library	Fluid Definition (Air Ideal Gas)
Fluid Definition	Material Library
Morphology	Continuous Fluid
Buoyancy Reference Density	$1.1685E + 0$ [kg/m^3]
Gravity Y Component	$-9.8100E + 0$ [m/s^2]
Gravity Z Component	$0.0000E + 0$ [m/s^2]
Reference Pressure	$1.0000E + 0$ [atm]
Turbulent Wall Functions	Automatic
High Speed Model	Off
Heat Transfer Model	Total Energy
Turbulence Model	SST/k-epsilon

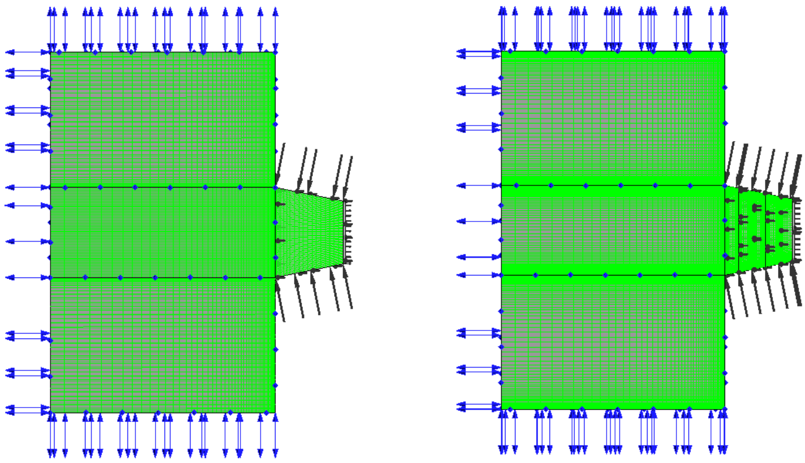

(a) Fluid Domain for Approach One

(b) Fluid Domain for Approach Two

Figure 26: Visual representations for the Fluid Domain pertaining to both Approaches

3.5.5 Air Inlet

The accuracy of the boundary conditions at the air inlet is highly important. By setting a mass flow rate condition, the amount of air entering the absorber can be controlled. This boundary condition not only allows for a realistic representation of the actual operating conditions but also provides a direct link to key performance metrics like the ARR and efficiency enabling to draw meaningful conclusions and make informed design decisions.

For all analyses related to approach one, it is assumed that the air inlet temperature will be set at 450 °C. Alongside the specified mass flow rate and adjusted temperature, a medium level of turbulence intensity has been selected. This parameter quantifies the degree of randomness in the airflow. For the analyses of approach two a mass flow gradient of the air inlet will be applied in the upcoming sections.

Table 4: Air Inlet Boundary Configurations

Type	**Inlet**
Flow Direction	Normal to Boundary Condition
Flow Regime	Subsonic
Heat Transfer	Static Temperature
Static Temperature	$4.5000E+2$ [°C]
Mass and Momentum	Bulk Mass Flow Rate
Mass Flow Rate	0.07 [kg/s]
Turbulence	Medium Intensity (Intensity=5%)
Fluid	Air Inlet

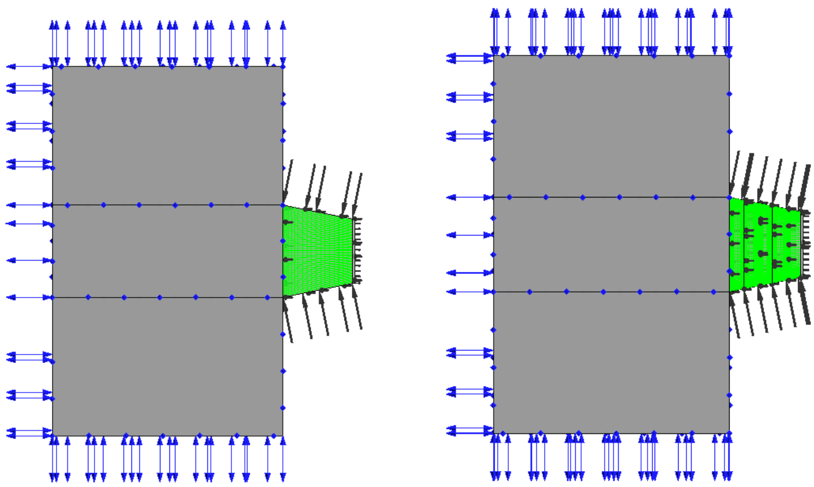

(a) Air inlet for Approach One **(b)** Air inlet for Approach Two

Figure 27: Visual representations for the air inlet conditions pertaining to both Approaches

3.5.6 Ambient

This condition plays role in defining the external environment surrounding the absorber. By setting a constant temperature of 22 °C and a relative pressure of 0 *bar* of the ambient for both approaches, a standardized reference point for the simulation is established. This choice is based on real-world conditions and provides a stable baseline against which the behavior of the absorber can be evaluated. By carefully specifying the ambient boundary condition, it is ensured that the simulation accurately reflects the interactions between the absorber and its surroundings, facilitating a comprehensive analysis of its performance. The choice of turbulence intensity and eddy viscosity ratio significantly influences the accuracy and realism of the simulations.

Turbulence intensity serves as a metric for quantifying the level of disorder within the turbulent flow, and it is expressed as a percentage of the free stream velocity. On the other hand, the eddy viscosity ratio offers insight into the relative magnitudes of turbulent viscosity compared to molecular viscosity. In the current context, a chosen value assumes that turbulent viscosity is tenfold higher than molecular viscosity, providing a basis for capturing the turbulent behavior with greater fidelity.

Table 5: Ambient Boundary Configurations

Type	**Opening**
Flow Direction	Normal to Boundary Condition
Flow Regime	Subsonic
Heat Transfer	Opening Temperature
Opening Temperature	$2.2000E + 1$ [°C]
Mass and Momentum	Opening Pressure and Direction
Relative Pressure	$0.0000E + 0$ [bar]
Turbulence	Intensity and Eddy Viscosity Ratio
Fluid	Air Inlet
Fractional Intensity	0.05
Eddy Viscosity Ratio	10

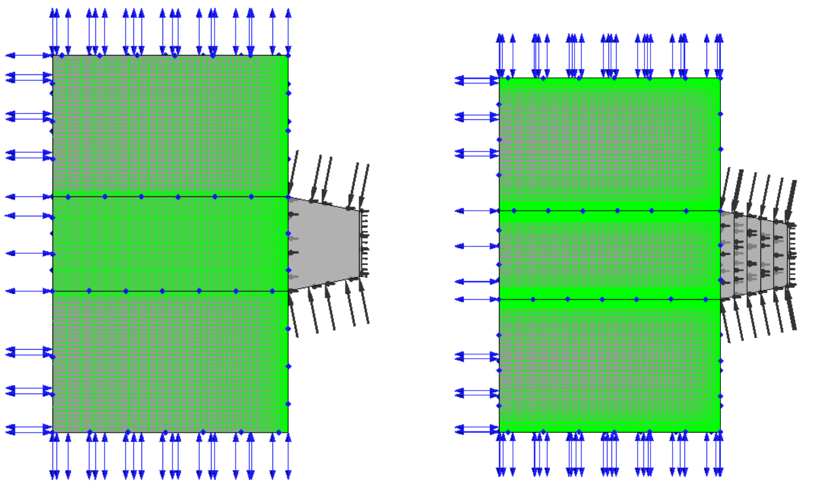

(a) Ambient for Approach One **(b)** Ambient for Approach Two

Figure 28: Visual representations for the ambient conditions pertaining to both Approaches

3.5.7 Wall

The wall boundary condition represents the scenario where fluid particles come into direct contact with a solid surface. This close interaction leads to a zero relative velocity between the fluid and the wall, enforcing a no-slip condition. This means that fluid molecules adhere closely to the surface, preventing any slippage or separation. By accurately representing this interaction through the wall boundary condition, the complexity of fluid-solid dynamics is captured.

Table 6: Wall Boundary Configurations

Type	**Wall**
Heat Transfer	Adiabatic
Mass and Momentum	No Slip Wall
Wall Roughness	Smooth Wall

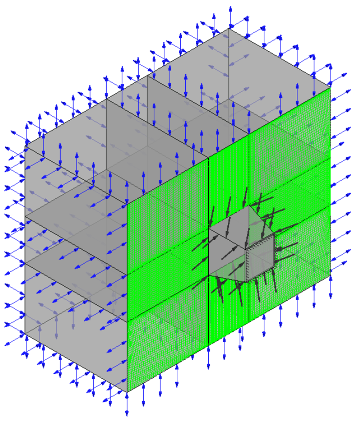

(a) Walls for Approach One

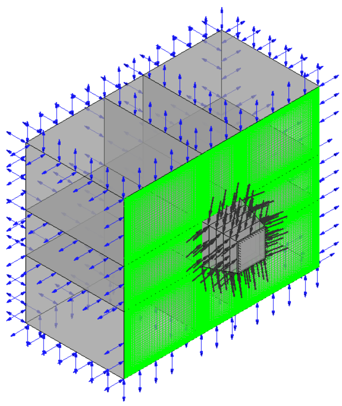

(b) Walls for Approach Two

Figure 29: Visual representations for the wall conditions pertaining to both Approaches

3.5.8 Porous Domain

The porous domain represents the portion that is filled with a porous material. The porous material is characterized by its porosity, which is the volume fraction of the void space in the material. For the analysis, a volumetric porosity of 0.5 is utilized. The flow of fluid through a porous medium is modeled using the Darcy-Forchheimer equation. This equation considers the effects of viscosity, permeability, and inertial forces. Viscosity is the property of a fluid that resists its flow. Permeability is a measure of how well a porous material allows fluid to flow through it. Inertial forces are the forces that arise from the fluid's motion.

Table 7: Porous Domain Boundary Configurations

Type	Porous
Material Library	Fluid Definition (Air Ideal Gas)
Fluid Definition	Material Library
Morphology	Continuous Fluid
Buoyancy Reference Density	$1.1685E + 0$ [kg/m^3]
Gravity X Component	$0.0000E + 0$ [m/s^2]
Gravity Y Component	$-9.8100E + 0$ [m/s^2]
Gravity Z Component	$0.0000E + 0$ [m/s^2]
Reference Pressure	$1.0000E + 0$ [atm]
Permeability	$7.59E - 7[m^2]$
Volume Porosity	0.5
Resistance Loss Coefficient	$6.47E + 0$ [1/m]
Heat Transfer Model	Total Energy
Turbulence Model	SST/k-epsilon

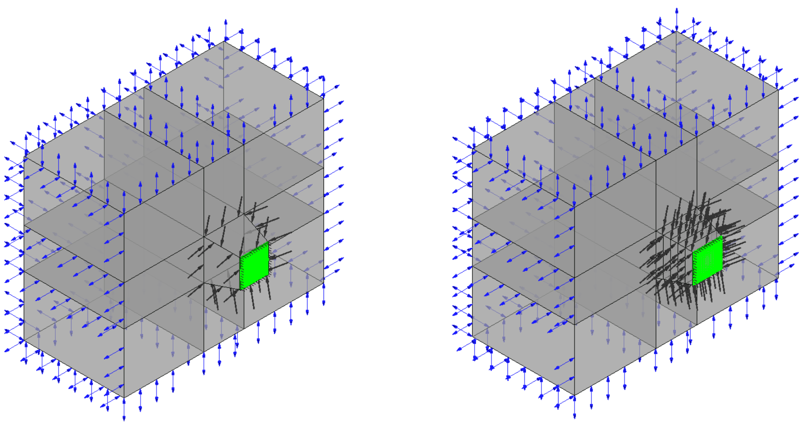

(a) Porous Domain for Approach One

(b) Porous Domain for Approach Two

Figure 30: Visual representations for the porous domain pertaining to both Approaches

3.5.9 Air Outlet

By setting a constant bulk mass flow rate at the outlet, a well-defined parameter that governs the flow of air exiting the absorber, the outlet boundary condition is defined. It serves as a key factor in determining the ARR and overall performance of the absorber. The constant mass flow is crucial for accurately assessing the system's efficiency and heat transfer capabilities.

In contrast, for approach two, the introduction of a mass flow gradient at both the air inlet and outlet adds a dynamic element to the simulations. This variation in flow conditions allows to thoroughly examine how the absorber reacts to different operating scenarios.

Table 8: Outlet Boundary Configuration

Type	**Outlet**
Heat Transfer	Adiabatic
Flow Regime	Subsonic
Mass and Momentum	Bulk Mass Flow Rate
Mass Flow Rate	0.07 [kg/s]

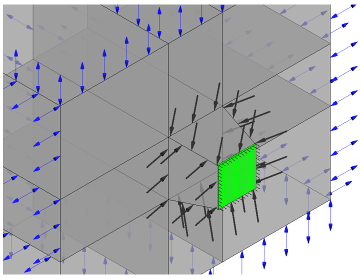

(a) Air Outlet for Approach One

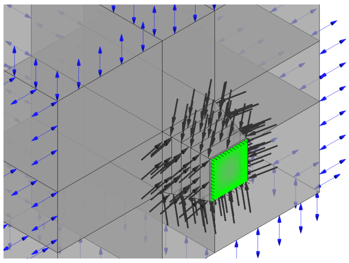

(b) Air Outlet for Approach Two

Figure 31: Visual representations for the air outlet conditions pertaining to both Approaches

4 Results

The assessments in this chapter are based on computational flow simulations performed using ANSYS CFX. The data under examination is obtained from steady-state RANS computations using the CFD setup described. The post processing of the effects and results were conducted and analyzed using CFX post. These effects will be represented visually on the models using contour plots and gradients of different flow quantities found in the output data set. This will enable the visualization and examination of the air as it enters the receiver and exits the main absorber. By comparing the ARR values of the different geometric alterations for the designed receivers, it can be determined which variation is the most beneficial in terms of both structural stability and efficiency. This will enable us to draw conclusions about the effects of geometry adaptations and the resulting consequences of mass flow and temperature gradients in the future.

To have a productive discussion about the results, it is important to choose the right turbulence model. In this thesis, the RANS based k-omega-SST and k-epsilon models are being compared, considering their respective advantages. Then a selection will be made to determine the most suitable model for further investigations.

After identifying the most favorable geometric variation using the simulation results, this section will delve into examining the impacts of applying both a mass flow gradient and a temperature gradient on the ARR of the receiver.

4.1 ARR Calculations

The definition of the ARR captures the fundamental principle of this innovative model. With surface temperatures reaching up to 1000 °C, the receiver captures the intense energy of sunlight, preparing the way for an exceptional thermal exchange process. The flow of air through the absorber modules acts as a channel for transferring the high thermal energy to a heat ex-changer or storage unit. Given the relatively low capacity of air to hold heat, large amounts of air must be circulated to effectively carry out this process.

The high mass flow requirement is a crucial in the design and operation of the system. It highlights the role that fluid dynamics play in ensuring its efficiency and overall performance. The ARR, which is a key performance metric, quantifies how effective this heat transfer process is. It provides a measure of the system's ability to convert solar energy into useful thermal power.

$$ARR = \frac{\dot{m}_{\text{ReturnedInletAir}}}{\dot{m}_{\text{HotAir}}} \tag{4.33}$$

Equation 4.33 provides a crucial measure of the system's efficiency in utilizing and recycling the heated air for further energy transfer.

4.2 Turbulence Model Selection

The ARR was calculated for both the k-epsilon and k-omega-SST turbulence model using the following expression in CFX-Post: Inlet Air.massFlow()@Outlet/massFlow()@Outlet. For all the data generated, an inlet mass flow of 0.07 kg/s and an inlet temperature of 450 °C are applied. Analyzing the generated data allows for drawing conclusions about how different receiver depths affect the ARR. By comparing the ARR calculations using both turbulence models, it is evident from Table 9 that the highest ARR is achieved with an aperture depth of 150 mm. The reasons behind this outcome will be explained in the upcoming chapters.

Table 9: ARR calculations for the SST and k-epsilon turbulence models

h [mm]	ARR [%] (SST)	ARR [%] (k-epsilon)
50	87.66	87.80
100	92.90	93.01
150	94.53	94.33
200	93.24	93.50

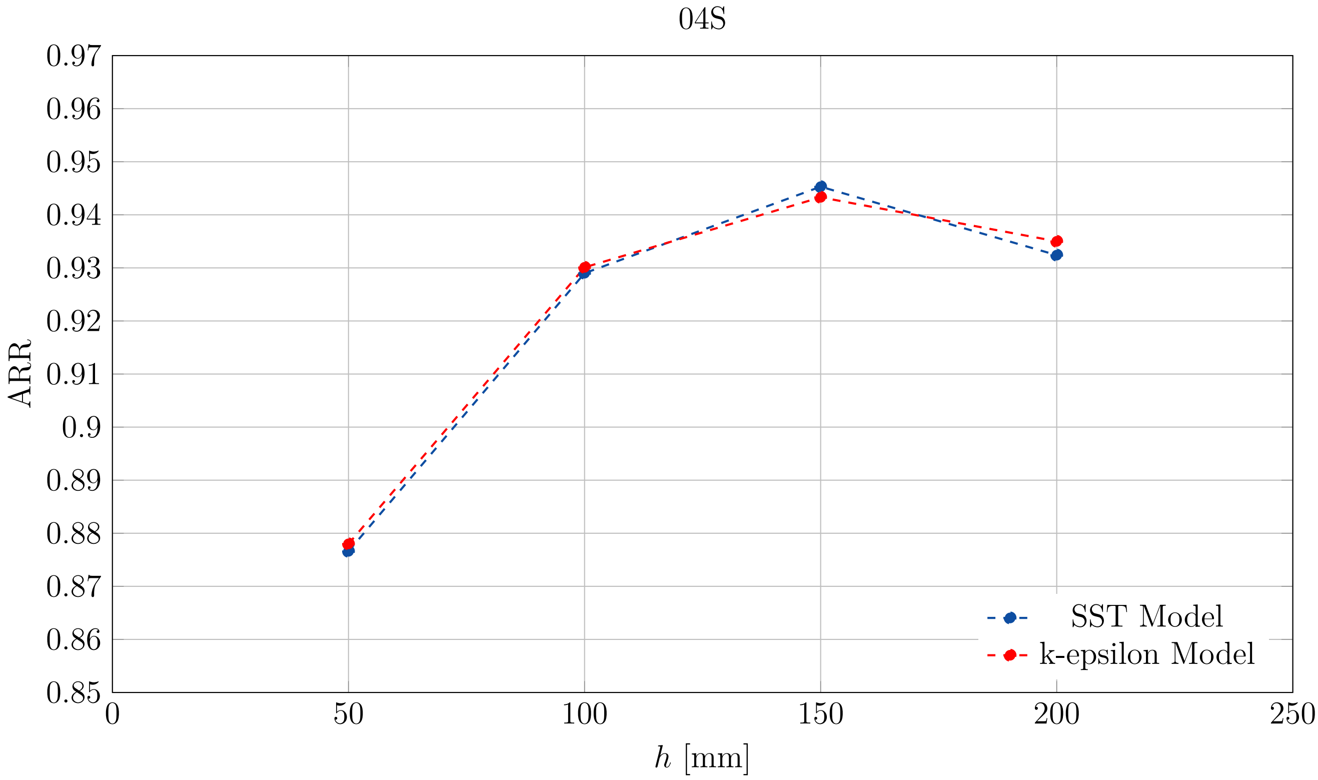

Figure 32: SST vs k-epsilon turbulence model

The calculated ARR for both the SST and k-epsilon models are closely aligned. This suggests a high degree of consistency in their predictions, which is a positive sign for their reliability in practical applications. It also indicates that both models are likely capturing the underlying physics of the system with a similar level of accuracy.

Given the close alignment of the obtained ARR values, it is imperative to conduct additional research to determine which one is more suitable for future investigations regarding thermal efficiency and ARR analysis.

The SST model transitions to a traditional k-epsilon model when moving away from walls. Near walls, it uses the omega formulation, while the realizable k-epsilon model uses the epsilon formulation. These two models have different methodologies when it comes to both near and away from walls. The SST is commonly regarded as more effective near walls, but it does have limitations. When moving away from walls, it switches to the standard k-epsilon model instead of the realizable k-epsilon model. Figure 33 depicts the advantages and disadvantages of these two turbulence models to get a better understanding.

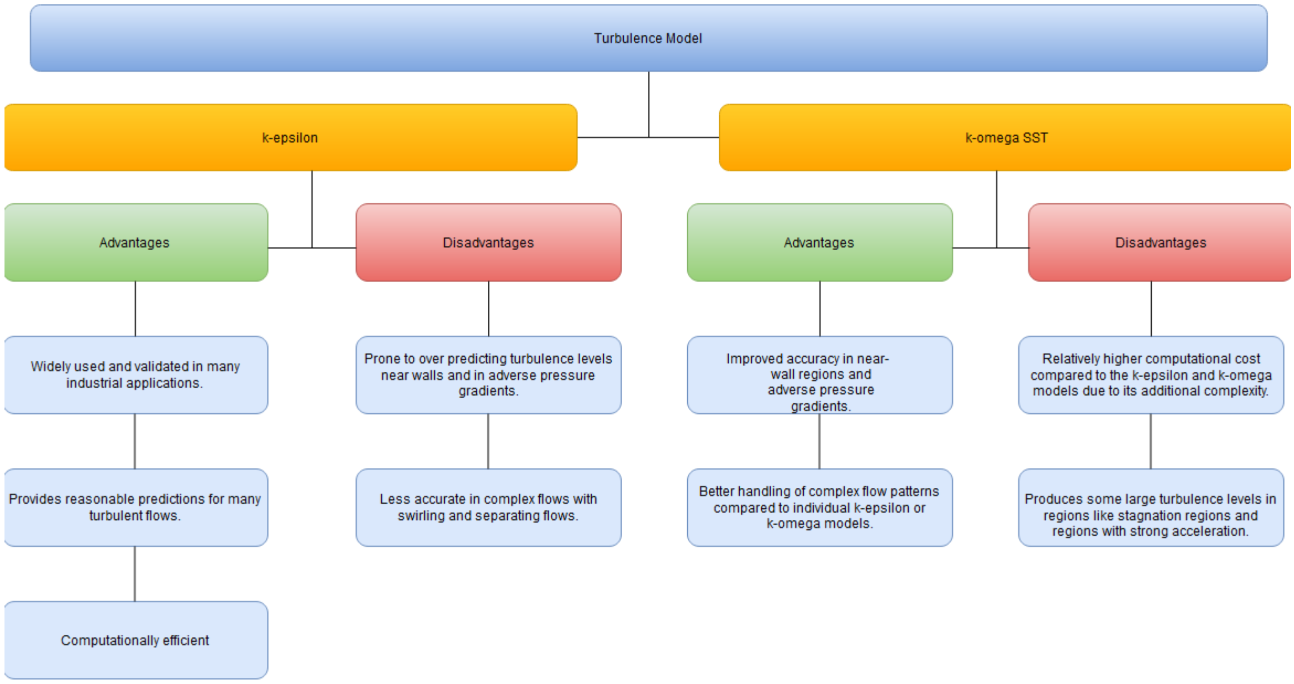

Figure 33: Comparison of k-epsilon and k-omega-SST

According to Figure 33, specific flow characteristics must be considerate for the selection. Factors like turbulence intensity, potential boundary layer separation, adverse pressure gradients, and the desired balance between precision and computational efficiency all play a role in this decision-making process.

After careful investigations, the decision to choose the SST model, after thoroughly evaluating its performance in comparison to the k-epsilon model, is based on its appropriateness for the multi-phase flow conditions and near wall treatment. This choice is particularly critical, as it ensures that the simulations capture the complex interactions between different phases of the flow, providing a more faithful representation of the influence of the ambient and inlet air introduced in the simulations. Additionally, the superior accuracy of the SST model in proximity to walls addresses a crucial aspect of the study, where precise understanding of flow characteristics near boundaries is paramount. This careful model selection process establishes a strong basis for the following CFD computations, ensuring a more reliable and credible analysis of the system's behavior.

4.3 Efficiency Calculations

Efficiency calculations were conducted to assess how effectively the receiver variations operate. An efficiency of 1, or 100 % if expressed as a percentage indicates a perfectly efficient system where all input is converted into useful output. In real-world scenarios, this is rarely achieved due to manifold losses of the receiver.In this scenario, the loss of energy through emission (which includes convective and radiation losses). In the context of this thesis the convective efficiencies of the respective receivers will be derived.

Convective efficiency specifically relates to how well the air inside the receiver cavity absorbs heat from the concentrated solar radiation. It is influenced by factors such as the design of the receiver, the flow patterns of the air inside the cavity, and the thermal properties of the materials used.

High convective efficiency means that a larger portion of the incident solar energy is effectively transferred to the air inside the cavity, which can then be used for various applications like generating steam for power generation, heating air for industrial processes, or other thermal applications.

There are various approaches to compute the convective efficiency of a system. The efficiency ratios for this thesis are computed using the return efficiency approach which is outlined by A. Cheilytko, 2022 [6]. For this approach the previously calculated ARR values for the k-omega SST turbulence model (Table 9) will be used. Additionally, the enthalpy values for the ambient and inlet air, derived from the heat atlas [25], are employed. The enthalpy values are primarily dependend on the temperatures of the air as ideal gas which is 22 °C for the ambient and 450 °C for the inlet. At these respective states the enthalpys are respectively -3,01 kJ/kg and 440,330 kJ/kg.

$$Q_{full} = Q_{useful} + Q_{loss} \tag{4.34}$$

$$1 = \eta_{\text{conv}} + \frac{Q_{\text{loss}}}{Q_{\text{full}}} \tag{4.35}$$

$$\eta_{\text{conv}} = 1 - q_{\text{loss}}^{\text{air}} \tag{4.36}$$

Equation 4.34 to Equation 4.36 outlines the derivation of the return efficiency method, wherein the convective heat loss, denoted as $q_{\text{loss}}^{\text{air}}$, is subtracted from 1. This resultant value is then interpreted as the convective efficiency of the receiver. Eqauation 4.39, can be used to compute $q_{\text{loss}}^{\text{air}}$ once the necessary values I_{rec} and $Q_{\text{loss}}^{\text{air}}$ are acquired for the system.

$$q_{\text{loss}}^{\text{air}} = \frac{Q_{\text{loss}}^{\text{air}}}{I_{\text{rec}}} \tag{4.37}$$

I_{rec} represents the amount of sunlight irradiation received on the receiver's surface, determined by the aperture length of the receiver. Given that the aperture length remains consistent across all variations of the receiver, I_{rec} remains constant for all receivers. The previously computed incoming solar radiation directed at the receiver was established at 800 kW/m^2 in STJ.

$Q_{\text{loss}}^{\text{air}}$ is the energy loss with the heat from the air leaving the solar plant to the environment and ϵ is a delay factor related to the time required to heat the exhaust air to a given temperature, which will be taken 1 for the upcoming calculations (stationary case).

$$Q_{\text{loss}}^{\text{air}} = \left(H_{\text{out}}^{\text{air}} - H_{amb}^{air}\right) \cdot (1 - ARR) \cdot \varepsilon \tag{4.38}$$

$H_{\text{out}}^{\text{air}}$ - enthalpy carried by air (kJ/s);

H_{amb}^{air} - enthalpy brought in with ambient air (kJ/s);

ε - delay factor.

Upon incorporating the computed values along with the ARR values acquired, the corresponding convective efficiency values for the different geometric variations are presented below:

Table 10: Convective efficiency distribution

h [mm]	η[%]
50	88.03
100	93.11
150	94.69
200	93.44

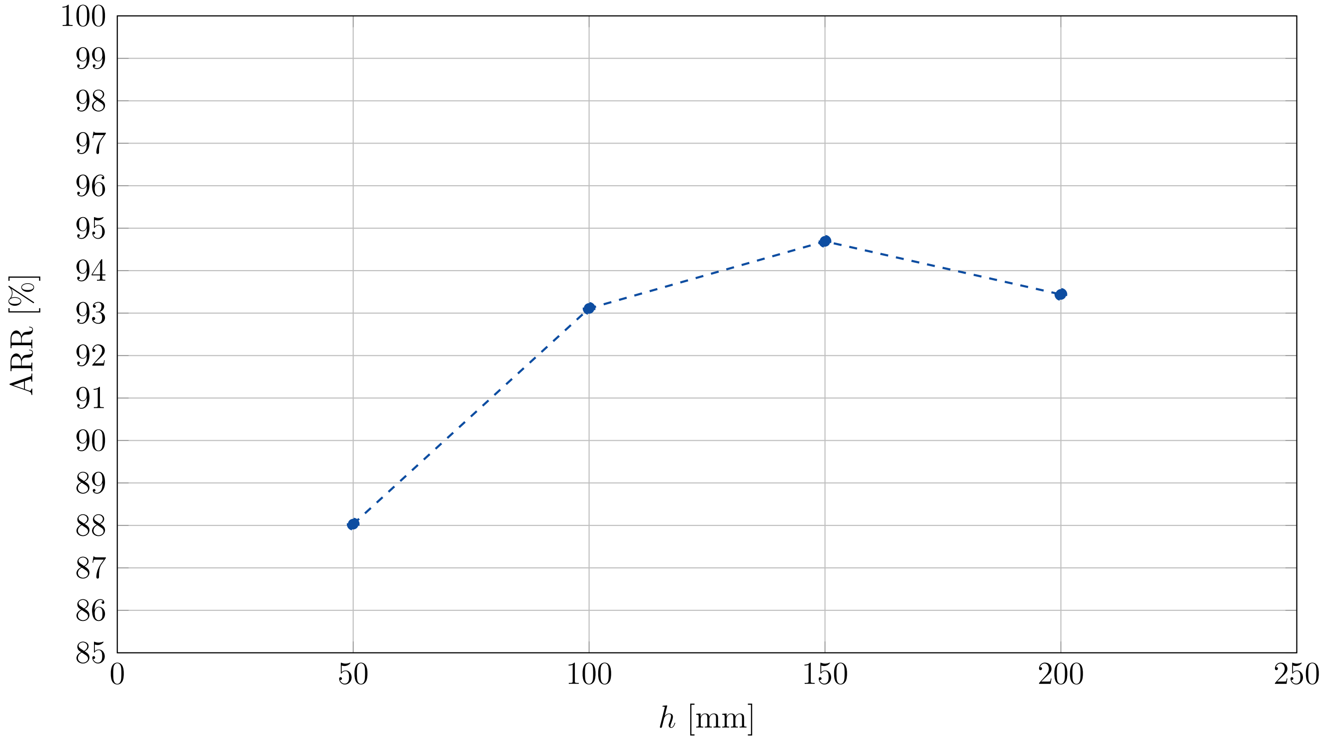

Figure 34: Convective efficiency distribution

The observed proportional relationship between ARR and convective heat efficiency is a noteworthy finding. This suggests that as the ARR increases or decreases, there is a corresponding change in the convective efficiency of the system. Such a correlation is of significant practical importance, as it implies that optimizing for one parameter could potentially lead to improvements in the other or vice versa. Understanding this proportional relationship can lead to more informed and efficient design choices. The geometric variation featuring a depth of 150 *mm*, which yielded the highest ARR, also demonstrates the most favorable performance in terms of convective efficiency.

4.4 Effect of Varied Load Scenarios

Changing the load for an open volumetric cavity receiver can affect the ARR. When the load is altered, it can influence factors such as airflow dynamics and heat transfer within the receiver. This, in turn, may lead to variations in the proportion of air that is returned to the system compared to the total air input.

Enhancing the ARR is advantageous in achieving optimal receiver efficiency as stated before. This efficiency is directly related to the mass flow rate of the air being returned, as indicated by Equation 4.33. To explore the impact of inlet mass flow on the ARR, the load distribution variation and their corresponding difference calculations between inlet mass flow and outlet mass flow across the receiver were examined for a aperture depth of 150 mm.

Furthermore, analyzing the load difference provides valuable insights into the system's operational characteristics. This metric, computed by subtracting the inlet mass flow from the outlet mass flow and then dividing it by the outlet mass flow (as per Equation 4.39), aids in understanding how efficiently the system is utilizing its resources. The calculations encompassed three specific mass flow rates: full load, 75% load, and 50% load. By incorporating these values into the equations, the resulting ARR distribution is presented in Table 11 and illustrated in Figure 35. This comprehensive assessment allows for a detailed evaluation of the system's performance under varying load conditions.

$$\delta_{\dot{m}_{\text{in}}} = \frac{\dot{m}_{\text{out}} - \dot{m}_{\text{in}}}{\dot{m}_{\text{out}}} \tag{4.39}$$

$$\dot{m}_{\text{in}} = \dot{m}_{\text{out}} \cdot \delta \dot{m}_{\text{in}} - \dot{m}_{\text{out}} \tag{4.40}$$

$$\dot{m}_{\text{in}} = \dot{m}_{\text{out}} \cdot (1 - \delta \dot{m}_{\text{in}}) \tag{4.41}$$

Load	**ARR** ($\delta min = 0\%$)	**ARR** ($\delta min = 5\%$)	**ARR** ($\delta min = 10\%$)
Full Load	%94.53	%91.53	%87.97
75% Load	%91.58	%90.05	%86.20
50% Load	%88.49	%85.43	%80.96

Table 11: Distribution of ARR for varied load fluctuations at a 150 mm aperture depth

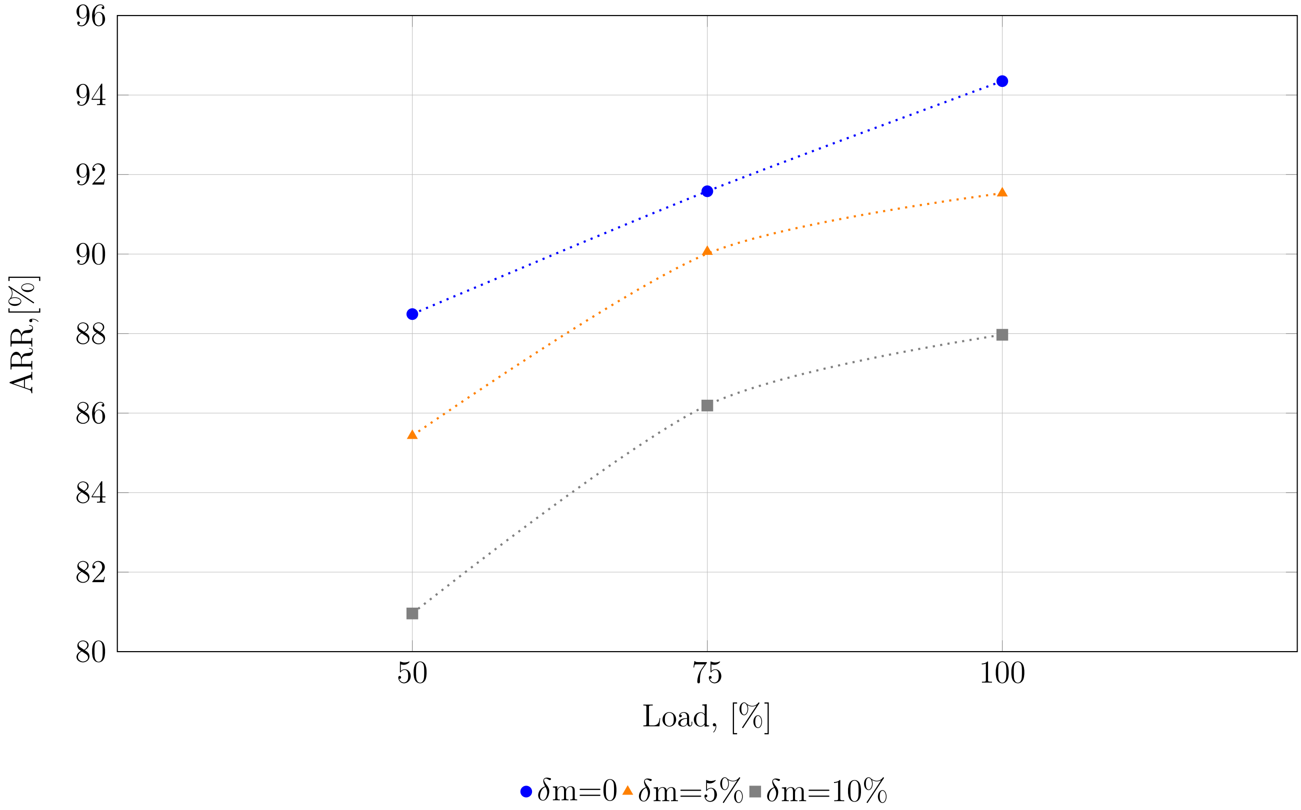

Figure 35: ARR distribution for different load variations

The relationship between mass flow rates and system performance underscores the need for a careful analysis of this parameter. As observed in Figure 35, the system's efficiency is linked to the mass flow rates. At full load, where the ARR reaches its peak without any deviation in mass flow outlet, the system operates at its maximum potential. However, as the mass flow rate diminishes down the receiver, there is a corresponding reduction in the overall ARR, ultimately leading to a decrease in the system's overall efficiency. This emphasizes the critical importance of fine-tuning and optimizing mass flow rates to achieve the highest possible performance in the system.

4.4.1 Analysis of the Effect of Receiver Depth on the ARR

In this section of the thesis, an examination will be conducted focusing on the ARR concerning receiver depths of different variations. This analysis will be facilitated through the generation of streamlines representing the inlet air velocity. This visualization technique will offer a deeper understanding of how varying receiver depths impact the ARR. As losses increase, ARR decreases, thus efficiency decreases. A trend is noticeable that the heat dissipation to the ambient decreases steadily up to a receiver depth increase of 150 mm, but then starts to rise again. These streamlines validate the accuracy of the earlier calculations for the ARR. This indicates a critical point at a depth of 150 mm, beyond which the warm air loss to the ambient begin to increase once more.

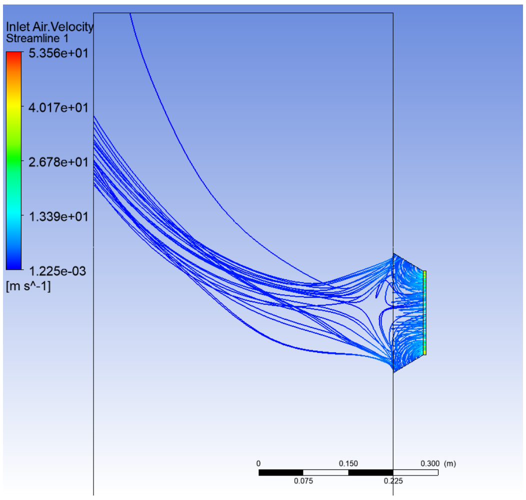

(a) Partial loss of warm air to the ambient for 50 mm aperture depth

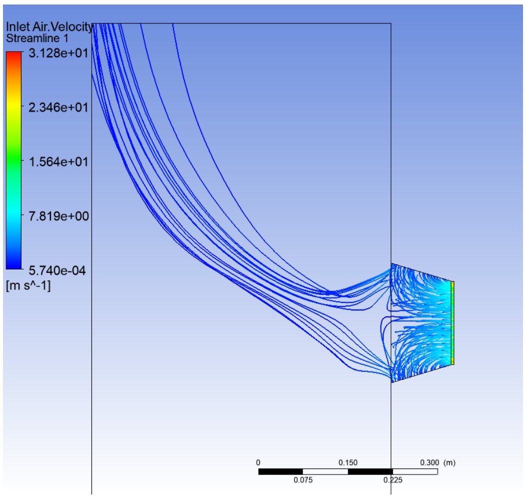

(b) Partial loss of warm air to the ambient for 100 mm aperture depth

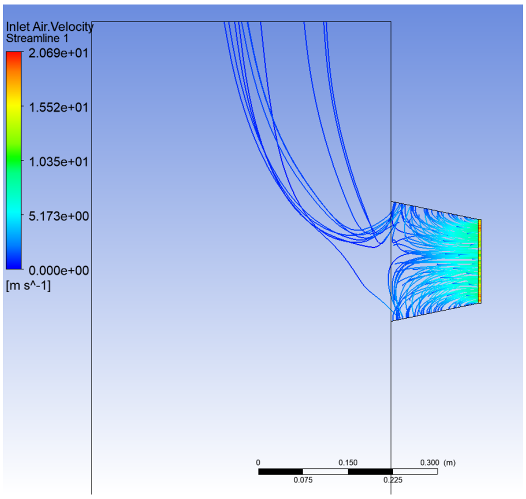

(c) Partial loss of warm air to the ambient for 150 mm aperture depth

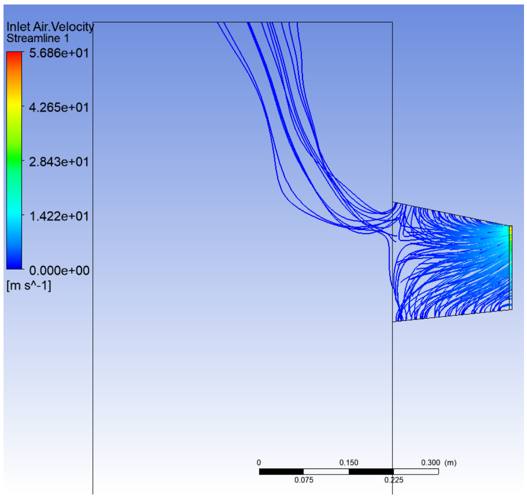

(d) Partial loss of warm air to the ambient for 200 mm aperture depth

Figure 36: Comparison of the partial loss of warm air to the ambient for different geometry variations

The analysis focuses on understanding the partial loss of warm air from the receiver to the surrounding environment, aiming to discern the factors influencing the alteration in the ARR. Investigating buoyancy becomes crucial in comprehending environmental losses. According to the conservation of mass, within a defined volume, the rate of mass change is zero.

$$\frac{\mathrm{d}M}{\mathrm{d}t} = \frac{\mathrm{d}}{\mathrm{d}t}\int \rho_f \ \mathrm{d}V = 0 \tag{4.42}$$

As the volume increases, density decreases, resulting in minimal fluctuations in the buoyancy force across variations in the receiver.

$$F_b = \int \rho_f g dV \tag{4.43}$$

$$F_{b50\ \mathrm{mm}} \cong F_{b100\ \mathrm{mm}} \cong F_{b150\ \mathrm{mm}} \cong F_{b200\ \mathrm{mm}} \tag{4.44}$$

While the mass flow rate maintains consistency across different configurations, an intriguing inverse relationship emerges in the context of aperture depth variations. Notably, lower aperture depths are associated with increased velocity impulses, suggesting a more dynamic flow pattern. In contrast, as the aperture depth increases, the velocity impulse diminishes. This reduction in velocity impulse implies a more controlled and restrained flow, leading to the retention of a greater proportion of warm air within the receiver. The intricate interplay between aperture depth and velocity impulses becomes a critical factor in shaping the thermal behavior and efficiency of the system, underscoring the importance of a nuanced understanding of these dynamics in the design and optimization of the receiver concept.

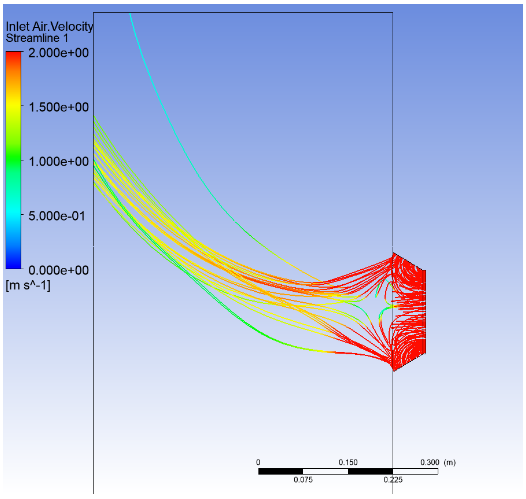

(a) Partial loss of warm air to the ambient for 50 mm aperture depth

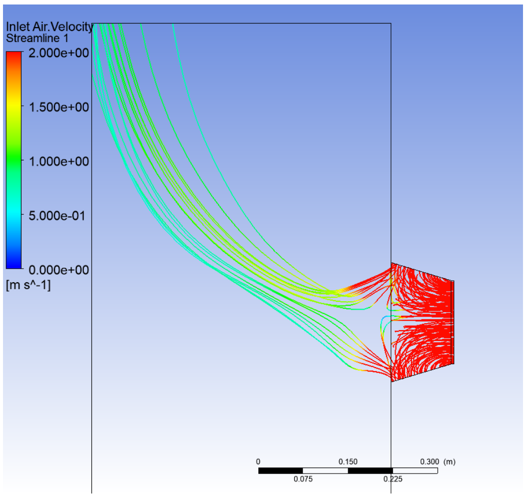

(b) Partial loss of warm air to the ambient for 100 mm aperture depth

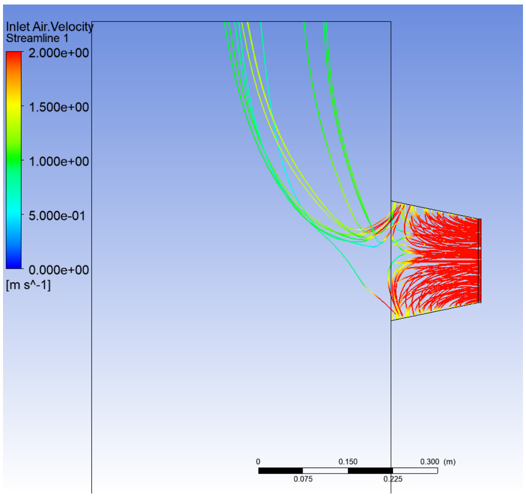

(c) Partial loss of warm air to the ambient for 150 mm aperture depth

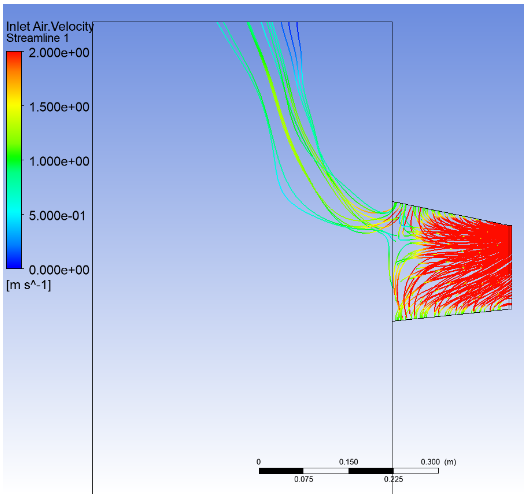

(d) Partial loss of warm air to the ambient for 200 mm aperture depth

Figure 37: Comparison of the partial loss of warm air to the ambient for different geometry variations

In exploring the changes in velocity impulse, the depiction of streamlines across a scale of 0 to 2 m/s offers a visual representation. The orientation of the velocity on the inlet surface is defined to be normal, perpendicular to the surface. Notably, as the aperture depths increase, there is a consistent reduction observed in both the inlet velocity and the angle theta.

$$I = \dot{m} \cdot u \cdot dt \tag{4.45}$$

$$I_y = \dot{m} \cdot u \cdot \sin(\theta) \cdot dt \tag{4.46}$$

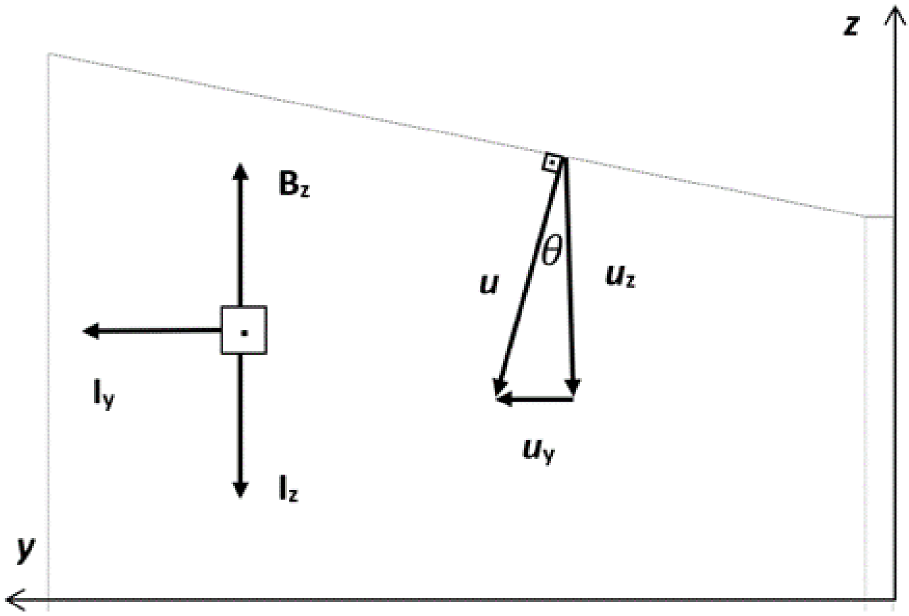

Figure 38: Visualization of the velocity vectors

This systematic decrease contributes to a corresponding reduction in velocity impulses along the y and z axes. This visualization enhances our understanding of how varying aperture depths influence the distribution of velocity impulses in different spatial dimensions.

h [mm]	Θ [°]	u [m/s]	$u \cdot \cos(\Theta)$ [m/s]
50	18.18	3.78	3.60
100	16.70	2.20	2.10
150	11.31	1.50	1.45
200	8.53	1.25	1.24

Table 12: Velocity variations across different aperture depths

When examining the internal flow within the cavity, a notable symmetry is observed along the centrifugal axis up to an aperture depth of 150 mm. However, as the aperture depth increases to 200 mm, a discernible asymmetry begins to manifest. This asymmetry has the potential to induce a reduction in the ARR, as it can significantly impact the recirculation phenomenon within the system.

4.5 Thermal Distribution Analysis

The thermal efficiency analysis will be interpreted by analysing the inlet total temperature contour plots. As the receiver contains an aperture, a portion of the exhausted air is naturally lost to the ambient and substituted with surrounding air as a consequence of the buoyancy effect [14] which can have a significant impact on the efficiency of a cavity air receiver. To analyse these effects the contour plots illustrated in Figure 39 will be utilized.

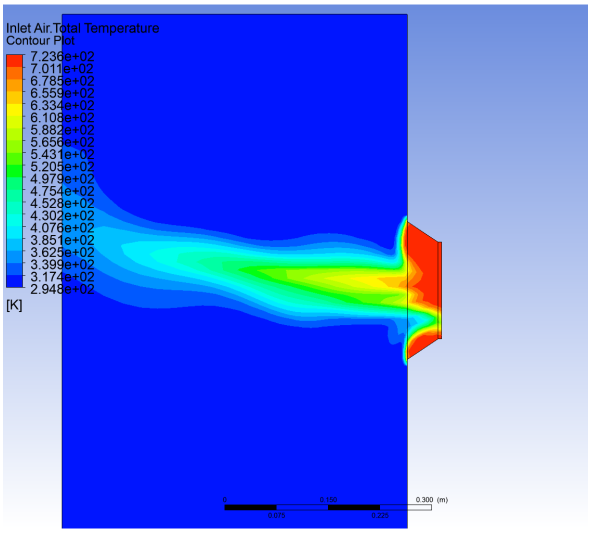

(a) Inlet total temperature contour for 50 mm aperture depth

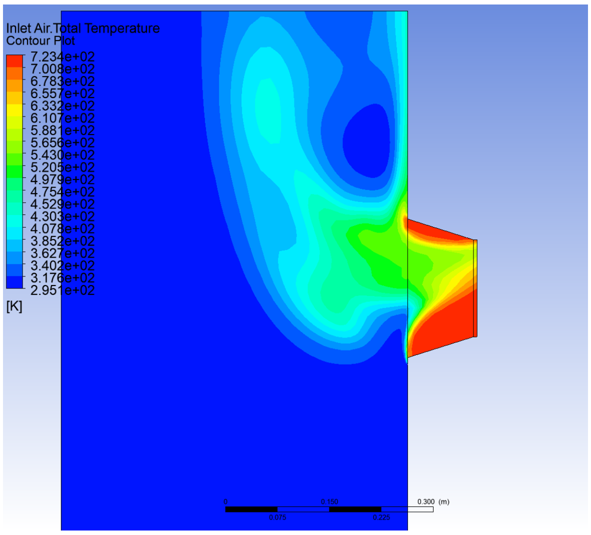

(b) Inlet total temperature contour for 100 mm aperture depth

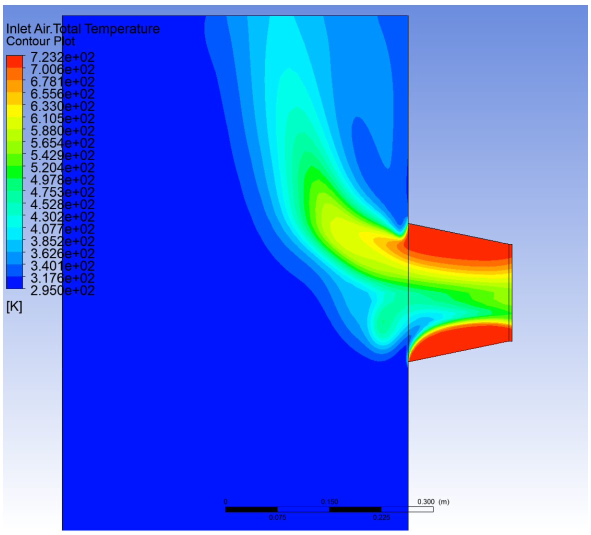

(c) Inlet total temperature contour for 150 mm aperture depth

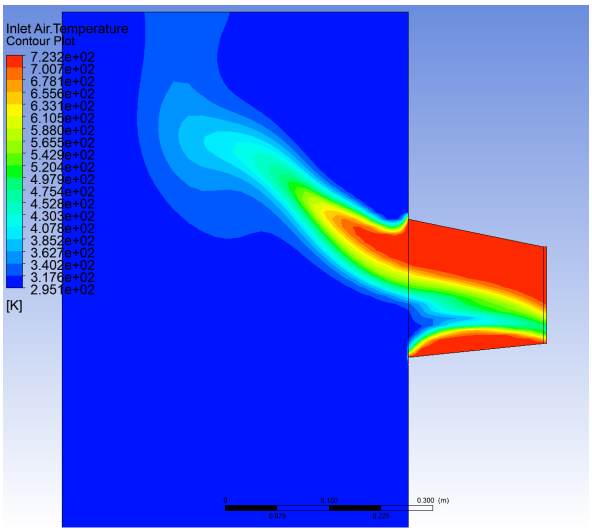

(d) Inlet total temperature contour for 200 mm aperture depth

Figure 39: Comparison of the inlet total temperature contour plots for the different geometry variations

The relatively hot air becomes less dense and rises due to buoyancy, this creates a natural flow circulation resulting with the cooler air entering at the bottom and warmer air rising to the top [18]. This circulation helps to distribute heat more evenly within the receiver, which can improve overall efficiency. It is evident from Figure 39 that the best heat distribution is achieved with a depth of 150 mm. The heat is almost evenly distributed over the walls of the receiver, contributing to maintain a more stable and efficient operation. For the other variations some localized overheating can be observed which can lead to potential structural damage. By maintaining more uniform temperatures, buoyant flow can help to reduce thermal stress on the receiver material which can lead to the a longer lifespan of the receiver and improve its overall reliability.

This analysis indicates that there is an optimal variation between the acting buoyancy forces and velocity impulse on the z direction of the receiver. With the investigations on the partial loss to the environment and the thermal analysis, the best performance is obtained with 150 mm aperture depth.

4.6 Analysis of the Gradient of Mass Flow and Temperature along the Receiver

In this section a clarification for the impact of both the mass flow gradient and the temperature gradient along the receiver surface will be made. These gradients will be incorporated into the receiver through two distinct approaches. In the initial scenario, there will be an increase to the main absorber, while in the subsequent case, an increase will be made to the aperture.

The examination of these gradients provides valuable insights into how variations in mass flow and temperature can influence the overall performance of the receiver system. By specifically targeting the main absorber and aperture, the aim is to gain a comprehensive understanding of the interaction between these factors and their effects on the system's efficiency limits. This investigation is important in optimizing the design and operation of the receiver for enhanced performance. As the maximum efficiency has been obtained for a receiver depth of 150 mm, the following analyzes will be based on this variation.

4.6.1 Mass Flow Gradient

To conduct the mass flow gradient analysis, the gradients will be introduced through two distinct orientations. Initially, adjustments will be made to the main absorber, followed by modifications to the aperture as illustrated in Figure 40.

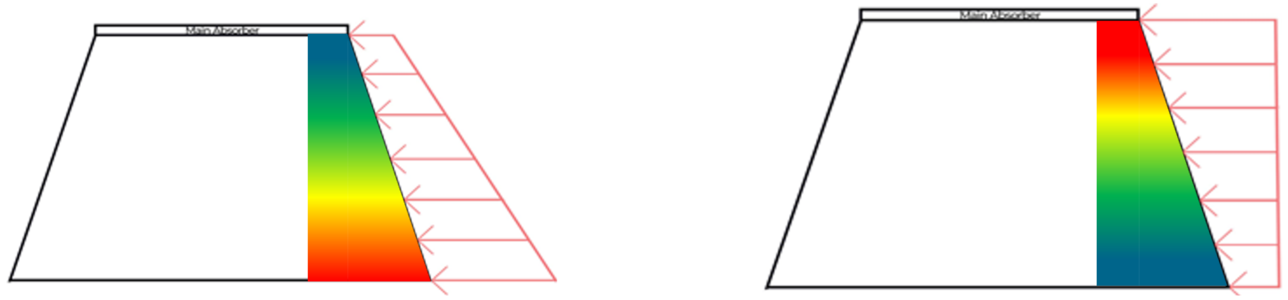

(a) Gradients Increasing to the aperture **(b)** Gradients Increasing to the main absorber

Figure 40: Illustration of the gradient orientation along the receiver

The variation in mass flow gradient, whether introduced to the main absorber or applied inversely on the aperture, is represented across different mass flow gradient percentage ranges. The mass flow gradients will be introduced at two varying levels, specifically 25% and 50% respectively for full load (0,0700 kg/s), 75% load (0,0525 kg/s), and 50% (0,0350 kg/s) load.

To exemplify the impact of the mass flow gradient, an observation is represented based on the utilization of the 150 mm receiver depth. The open cavity receiver is partitioned into five segments of uniform height. This division serves to implement the mass flow gradients for CFD simulations under different mass flow loads.

To enhance comprehension, Figure 41 assigns numerical labels to the segments utilized for the introduction of the mass flow gradients.

The mass flow for each segment are calculated as shown in Equation 4.47 for different loads:

$$\dot{m}_{\text{segment}} = \frac{\text{Area}_{\text{ segment}}}{\text{Area}_{\text{ total}}} \cdot \dot{m}_{\text{load}} \tag{4.47}$$

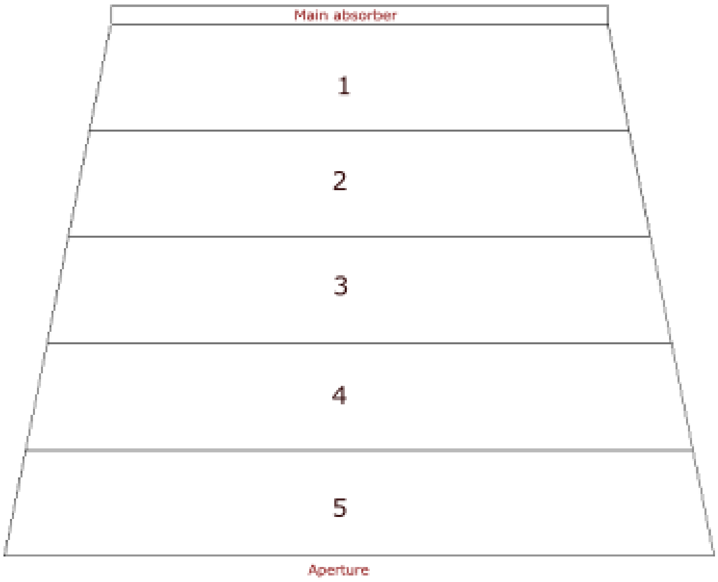

Figure 41: Number labeling of the segments

To verify the accuracy of the introduced mass flows, the corresponding mass flow densities are computed with the equation:

$$\dot{\mathrm{m}}_{\mathrm{density}} = \frac{\dot{\mathrm{m}}_{\mathrm{segment}}}{\mathrm{Area}_{\ \mathrm{segment}}} \tag{4.48}$$

Corresponding values indicating the variation in mass flow and the mass flow densities for the mentioned scenarios are provided in Tables below:

Table 13: Mass flow density distribution for full load

Section	**Uniform Mass Flow Density** [kg/s mm^2]	**50% gradient on Mass Flow Density to aperture** [kg/s mm^2]	**50% gradient on Mass Flow Density to the main absorber** [kg/s mm^2]	**25% gradient on Mass Flow Density to aperture** [kg/s mm^2]	**25% gradient on Mass Flow Density to the main absorber** [kg/s mm^2]
1	6,729E-07	3,364E-07	9,053E-07	5,047E-07	7,912E-07
2	6,729E-07	5,047E-07	8,411E-07	6,056E-07	6,729E-07
3	6,729E-07	6,729E-07	6,729E-07	6,729E-07	6,729E-07
4	6,729E-07	8,411E-07	5,047E-07	6,729E-07	6,056E-07
5	6,729E-07	9,053E-07	3,364E-07	7,912E-07	5,047E-07

Table 14: Mass flow distribution for full load

Section	Uniform Mass Flow [kg/s]	50% gradient on Mass Flow to aperture [kg/s]	50% gradient on Mass Flow to the main absorber [kg/s]	25% gradient on Mass Flow to aperture [kg/s]	25% gradient on Mass Flow to the main absorber [kg/s]
1	0,0120	0,0060	0,0214	0,0090	0,0187
2	0,0130	0,0097	0,0187	0,0117	0,0164
3	0,0140	0,0140	0,0140	0,0140	0,0140
4	0,0149	0,0187	0,0097	0,0164	0,0117
5	0,0159	0,0214	0,0060	0,0187	0,0090
Total Mass Flow	0,0700	0,0700	0,0700	0,0700	0,0700

Table 15: Mass flow density distribution for 75% load

Section	Uniform Mass Flow Density [kg/s mm^2]	50% gradient on Mass Flow Density to aperture [kg/s mm^2]	50% gradient on Mass Flow Density to the main absorber [kg/s mm^2]	25% gradient on Mass Flow Density to aperture [kg/s mm^2]	25% gradient on Mass Flow Density to the main absorber [kg/s mm^2]
1	5,047E-07	2,523E-07	6,790E-07	3,785E-07	5,551E-07
2	5,047E-07	3,785E-07	6,308E-07	4,54E-07	5,551E-07
3	5,047E-07	5,047E-07	5,047E-07	5,047E-07	5,047E-07
4	5,047E-07	6,308E-07	3,785E-07	5,551E-07	4,542E-07
5	5,047E-07	6,790E-07	2,523E-07	5,551E-07	3,785E-07

Table 16: Mass flow distribution for 75% load

Section	Uniform Mass Flow [kg/s]	50% gradient on Mass Flow to aperture [kg/s]	50% gradient on Mass Flow to the main absorber [kg/s]	25% gradient on Mass Flow to aperture [kg/s]	25% gradient on Mass Flow to the main absorber [kg/s]
1	0,0090	0,0045	0,0161	0,0067	0,0140
2	0,0097	0,0077	0,0140	0,0087	0,0123
3	0,0105	0,0105	0,0105	0,0105	0,0105
4	0,0112	0,0140	0,0077	0,0123	0,0087
5	0,0119	0,0161	0,0045	0,0140	0,0067
Total Mass Flow	0,0525	0,0525	0,0525	0,0525	0,0525

Table 17: Mass flow density distribution for 50% load

Section	Uniform Mass Flow Density [kg/s mm^2]	50% gradient on Mass Flow Density to aperture [kg/s mm^2]	50% gradient on Mass Flow Density to the main absorber [kg/s mm^2]	25% gradient on Mass Flow Density to aperture [kg/s mm^2]	25% gradient on Mass Flow Density to the main absorber [kg/s mm^2]
1	3,364E-07	1,682E-07	4,526E-07	2,523E-07	3,956E-07
2	3,364E-07	2,523E-07	4,205E-07	3,028E-07	3,701E-07
3	3,364E-07	3,364E-07	3,364E-07	3,364E-07	3,364E-07
4	3,364E-07	4,205E-07	2,523E-07	3,701E-07	3,028E-07
5	3,364E-07	4,526E-07	1,682E-07	3,956E-07	2,523E-07

Table 18: Mass flow distribution for 50% load

Section	Uniform Mass Flow [kg/s]	50% gradient on Mass Flow to aperture [kg/s]	50% gradient on Mass Flow to the main absorber [kg/s]	25% gradient on Mass Flow to aperture [kg/s]	25% gradient on Mass Flow to the main absorber [kg/s]
1	0,0060	0,0030	0,0107	0,0045	0,0093
2	0,0065	0,0048	0,0093	0,0058	0,0082
3	0,0070	0,0070	0,0070	0,0070	0,0070
4	0,0074	0,0093	0,0048	0,0082	0,0058
5	0,0079	0,0107	0,0030	0,0093	0,0045
Total Mass Flow	0,0350	0,0350	0,0350	0,0350	0,350

The mass flow densities for the load variations show that for each segment the introduced mass flows are evenly distributed across each section. The variation of the ARR with regards to the mass flow gradient, whether introduced to the main absorber (see positive values) or applied inversely to the aperture (see negative values) is represented in Figure 42.

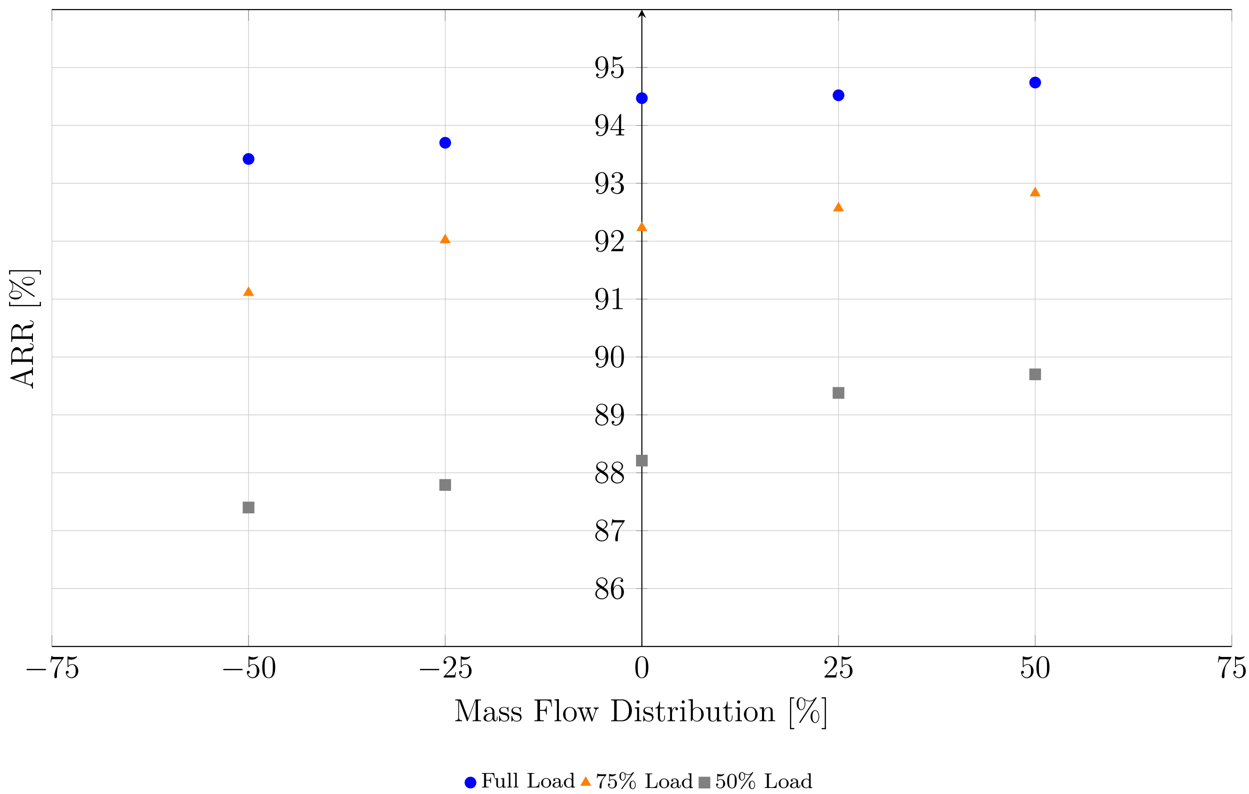

Figure 42: Mass flow gradient ARR distribution

Increasing the overall mass flow typically results in an increase of the ARR. Nevertheless, it also brings about reduced air temperatures, consequently leading to distinct operational states for the receiver. Hence, the ARR changes in the depicted cases will be evaluated under the same load variations. While this implies that fine-tuning the mass flow is important for increasing system efficiency, it indicates a direct connection between the orientation of the applied mass flow density along the inlet of the receiver. This underscores the significance of the system design for enhanced performance an examination of the cavity's internal dynamics is imperative. Given the relatively consistent inlet air velocities, the examination of warm air loss to the surroundings becomes important for meaningful comparisons.

From Figure 43, it can be stated that increasing the mass flow to the main absorber in an open volumetric cavity receiver mainly increases the ARR.

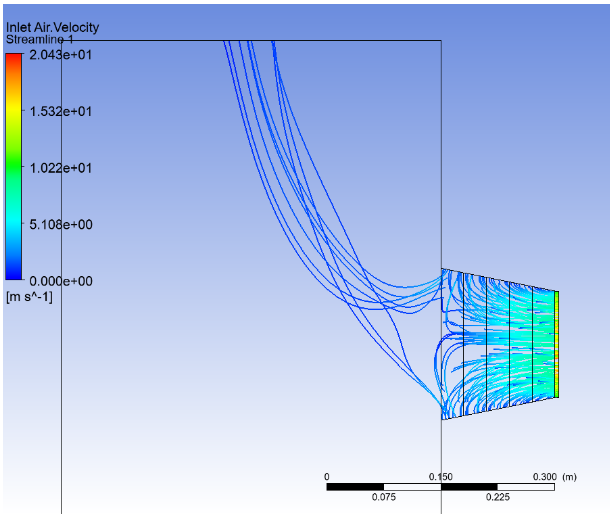

(a) Partial loss of warm air for 50% mass flow gradient to main absorber

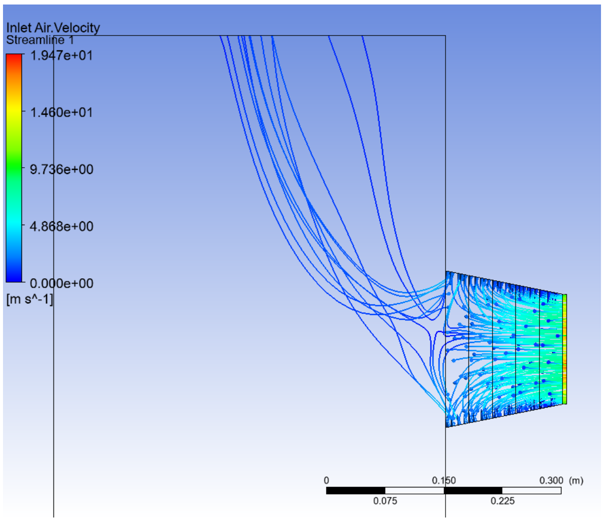

(b) Partial loss of warm air for 50% mass flow gradient to aperture

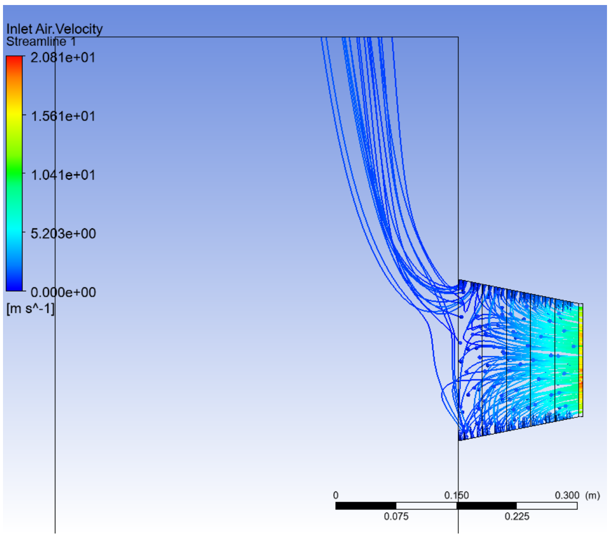

(c) Partial loss of warm air for 25% mass flow gradient to main absorber

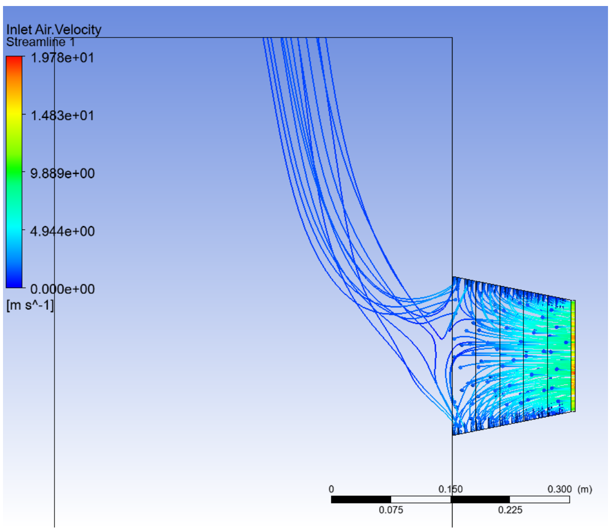

(d) Partial loss of warm air for 25% mass flow gradient to aperture

Figure 43: Comparison of the partial loss of warm air to the ambient for different geometry variations

Increasing the mass flow gradient to section 1 (the section closest to the main absorber) leading to higher ARR in the open volumetric cavity receiver can be explained by several factors:

- By increasing the mass flow gradient to section 1, more air is directed towards the main absorber. This leads to more effective convective heat transfer between the main absorber and the air, resulting in a higher proportion of recirculated air and an increased ARR.
- Since section 1 is closest to the main absorber, it plays a crucial role in capturing the maximum amount of heat. Increasing the mass flow gradient in this section ensures that a larger portion of the incoming air is exposed to the high-temperature absorber surface.
- Increasing the mass flow gradient to section 1 may help reduce heat losses at the aperture (section 5). A higher flow rate in section 1 can help confine more heat within the cavity, minimizing losses through the aperture.

Specifically, for a mass flow gradient distribution of 50%, the ARR experiences an reduction of roughly 1.5%, while for a distribution of 25%, it decreases by about 0.85%. This underscores the proportional decrease in ARR with increased mass flow near the aperture, as losses become more evident.

It's important to note that there are practical limits for increasing the mass flow gradients before encountering diminishing returns or other engineering constraints. These may include considerations like increased pressure drop across the system and potential limitations of the receiver design.

4.6.2 Temperature Gradient

The purpose of the temperature gradient is to facilitate the transfer of thermal energy from the concentrated sunlight absorbed by the receiver to the air passing through it. Here are the steps and considerations for applying a temperature gradient

Once more, the same method is applied that is used in the mass flow gradient approach, this time with the incorporation of the temperature gradients in both directions along the receiver with the implementation of uniform mass flows for different loads. The utilized temperature gradients are respectively 25°C, 50°C, and 75°C for varied load levels along the receiver for this analysis.

Table 19: Temperature gradient distribution for 25 °C

Section	Uniform Mass Flow for Full Load [kg/s]	25 °C temperature gradient to the main absorber [°C]	25 °C temperature gradient to the aperture [°C]
1	0,0120	475,0	425,0
2	0,0130	462,5	437,5
3	0,0140	450,0	450,0
4	0,0149	437,5	462,5
5	0,0159	425,0	475,0
Section	**Uniform Mass Flow for 75% Load [kg/s]**	**25 °C temperature gradient to the main absorber [°C]**	**25 °C temperature gradient to the aperture [°C]**
1	0,0090	475,0	425,0
2	0,0097	462,5	437,5
3	0,0105	450,0	450,0
4	0,0112	437,5	462,5
5	0,0119	425,0	475,0
Section	**Uniform Mass Flow for 50% Load [kg/s]**	**25 °C temperature gradient to the main absorber [°C]**	**25 °C temperature gradient to the aperture [°C]**
1	0,0060	475,0	425,0
2	0,0065	462,5	437,5
3	0,0070	450,0	450,0
4	0,0074	437,5	462,5
5	0,0079	425,0	475,0

Table 20: Temperature gradient distribution for 50 °C

Section	Uniform Mass Flow for Full Load [kg/s]	50 °C temperature gradient to the main absorber [°C]	50 °C temperature gradient to the aperture [°C]
1	0,0120	400,0	500,0
2	0,0130	425,0	475,0
3	0,0140	450,0	450,0
4	0,0149	475,0	425,0
5	0,0159	500,0	400,0
Section	**Uniform Mass Flow for 75% Load [kg/s]**	**50 °C temperature gradient to the main absorber [°C]**	**50 °C temperature gradient to the aperture [°C]**
1	0,0090	400,0	500,0
2	0,0097	425,0	475,0
3	0,0105	450,0	450,0
4	0,0112	475,0	425,0
5	0,0119	500,0	400,0
Section	**Uniform Mass Flow for 50% Load [kg/s]**	**50 °C temperature gradient to the main absorber [°C]**	**50 °C temperature gradient to the aperture [°C]**
1	0,0060	475,0	425,0
2	0,0065	462,5	437,5
3	0,0070	450,0	450,0
4	0,0074	437,5	462,5
5	0,0079	425,0	475,0

Table 21: Temperature gradient distribution for 75 °C

Section	Uniform Mass Flow for Full Load [kg/s]	75 °C temperature gradient to the main absorber [°C]	75 °C temperature gradient to the aperture [°C]
1	0,0120	375,0	525,0
2	0,0130	412,5	487,5
3	0,0140	450,0	450,0
4	0,0149	487,5	412,5
5	0,0159	525,0	375,0
Section	**Uniform Mass Flow for 75% Load [kg/s]**	**75 °C temperature gradient to the main absorber [°C]**	**75 °C temperature gradient to the aperture [°C]**
1	0,0090	375,0	525,0
2	0,0097	412,5	487,5
3	0,0105	450,0	450,0
4	0,0112	487,5	412,5
5	0,0119	525,0	375,0
Section	**Uniform Mass Flow for 50% Load [kg/s]**	**75 °C temperature gradient to the main absorber [°C]**	**75 °C temperature gradient to the aperture [°C]**
1	0,0060	375,0	525,0
2	0,0065	412,5	487,5
3	0,0070	450,0	450,0
4	0,0074	487,5	412,5
5	0,0079	525,0	375,0

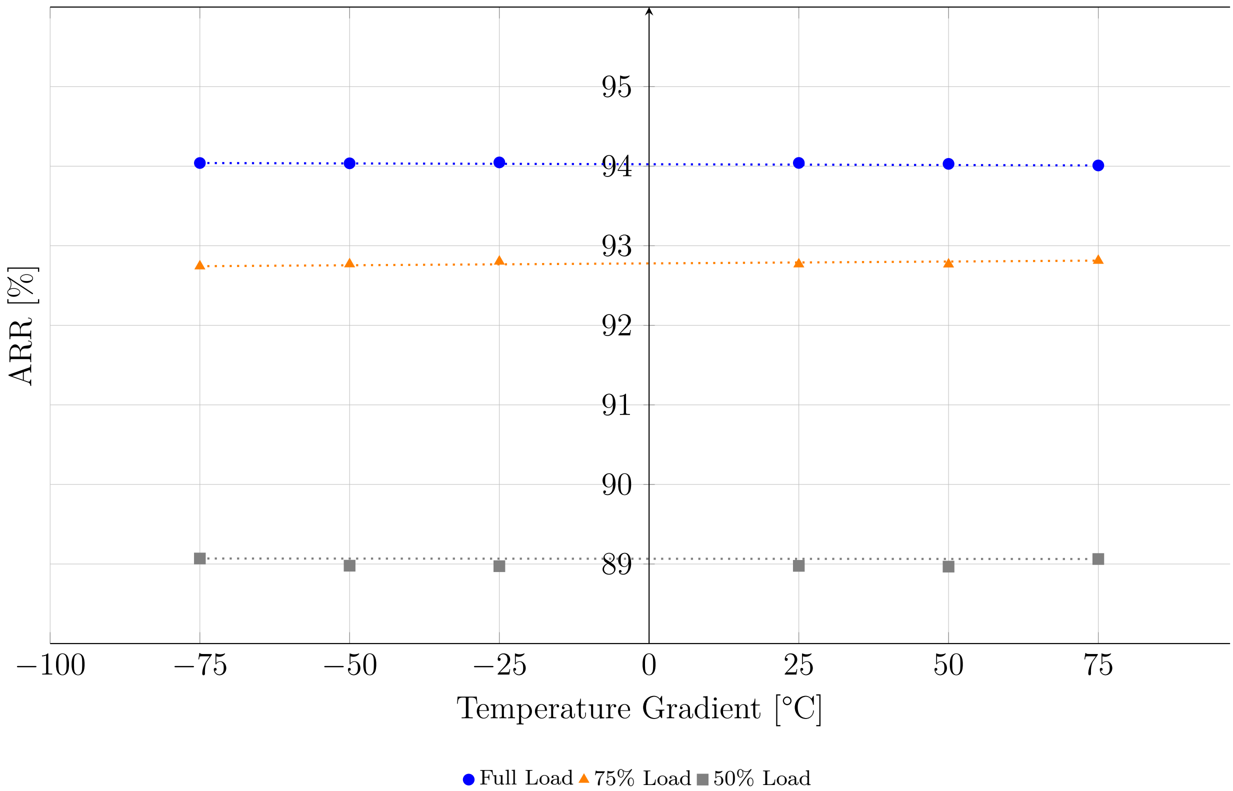

Figure 44: ARR dependence on the temperature gradient

Figure 44, shows the ARR values obtained for different loads. It can be observed that incorporating a temperature gradient, by keeping the inlet mass flow constant, has almost no effect on the ARR distribution for the same load distributions.

The observed contour plots for the inlet total temperature in Figure 45 show the interaction between the implemented temperature gradient and the thermal dynamics within the receiver. The temperature gradient's applied on the regions in close proximity to the walls underscores the significance of boundary conditions in governing heat transfer processes. This localized impact displays as a noticable deviation from uniform temperature distribution, leading to variations in thermal gradients along the receiver's periphery. Conversely, the internal regions exhibit a relatively stable temperature profile. This decoupling between the external and internal temperature distributions show the overall influence on buoyancy forces, indicating that while the gradient exerts a notable effect near the walls, its effect on the system's thermal behavior remain limited.

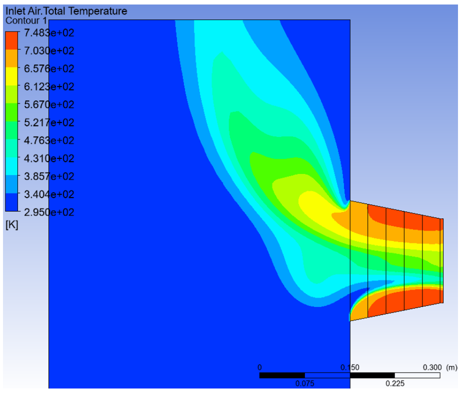

(a) Contour plot for 25 °C temperature gradient to the main absorber

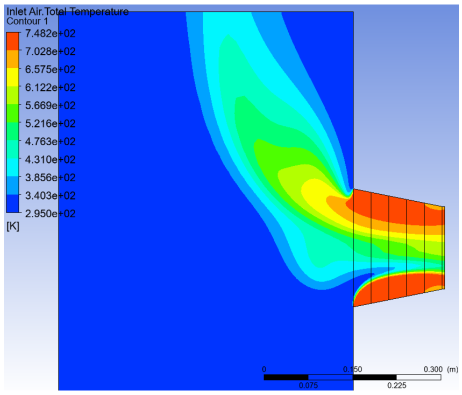

(b) Contour plot for 25 °C temperature gradient to aperture

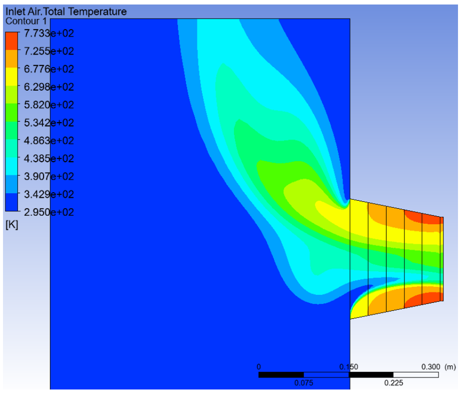

(c) Contour plot for 50 °C temperature gradient to the main absorber

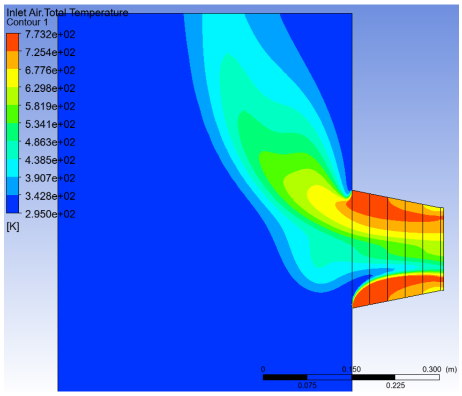

(d) Contour plot for 50 °C temperature gradient to aperture

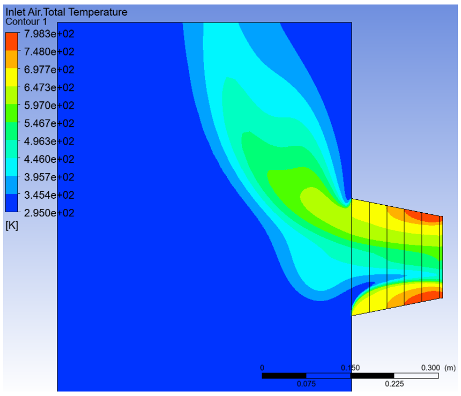

(e) Contour plot for 75 °C temperature gradient to the main absorber

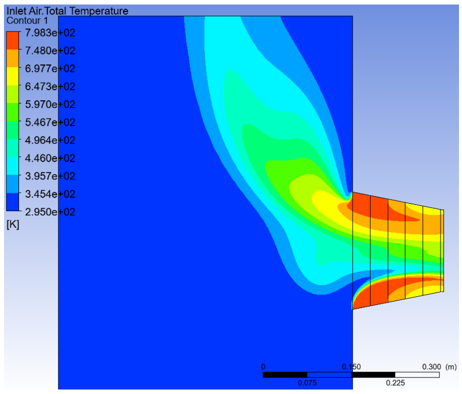

(f) Contour plot for 75 °C temperature gradient to aperture

Figure 45: Comparison of the inlet air total temperature contour plots for different temperature gradients

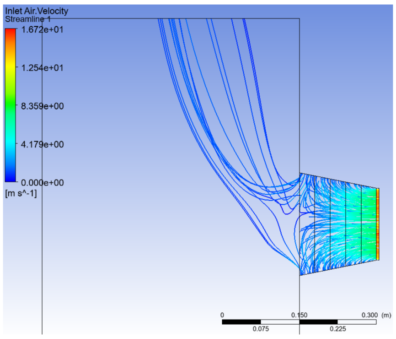

(a) Partial loss of warm air for 25 °C temperature gradient to the main absorber

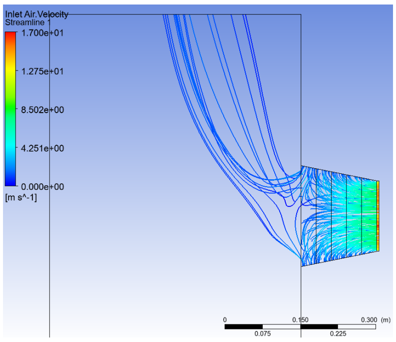

(b) Partial loss of warm air for 25 °C temperature gradient to aperture

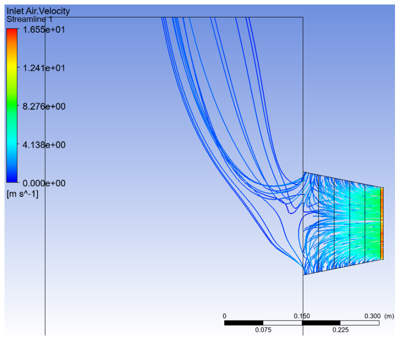

(c) Partial loss of warm air for 50 °C temperature gradient to the main absorber

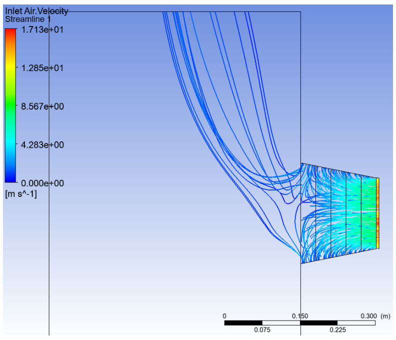

(d) Partial loss of warm air for 50 °C temperature gradient to aperture

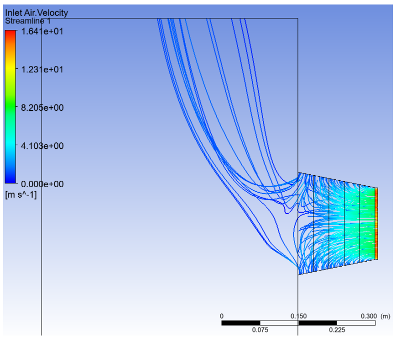

(e) Partial loss of warm air for 75 °C temperature gradient to the main absorber

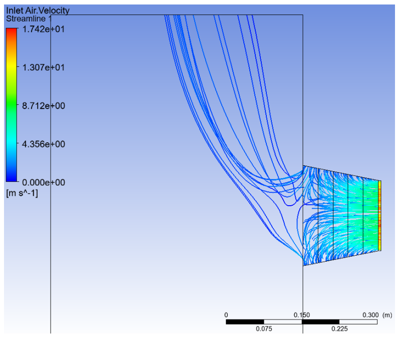

(f) Partial loss of warm air for 75 °C temperature gradient to aperture

Figure 46: Comparison of the partial loss of warm air to the ambient for different temperature gradients

The consistent behavior in losses to the surroundings serves as a crucial insight for the implementation of the temperature gradient. While alterations in geometry or the introduction of mass flow gradients can impact the receiver's performance, the near-constant losses to the surroundings provide a stable baseline against which other design modifications can be assessed. This inherent stability in the losses signifies a degree of resilience in the system, suggesting that even in the face of external perturbations or variations in operating conditions, the ARR can maintain its operational integrity. This characteristic is particularly valuable in real-world applications where the receiver may encounter dynamic and unpredictable environments, underlining the importance of considering not only design enhancements but also the inherent stability of the system in achieving optimal performance.

It is worth noting that the constant dissipation of heat to the ambient is a favorable outcome, as it signifies a stable thermal performance regardless of the applied temperature gradient. The depicted figures show that the implemented temperature gradient influences the temperature distribution in proximity to the walls, but exerts minimal influence on the internal regions of the receiver. Consequently, this has a limited impact on the overall buoyancy forces and overall losses to the environment. Moreover, the heat dissipated to the surroundings remains nearly constant across all scenarios. If CFD simulations have shown that implementing a temperature gradient with constant mass flow has no effect on the air return ratio in the open volumetric cavity receiver, there could be several potential reasons for this outcome:

- The design of the receiver or the flow patterns of the air may not allow for significant interaction between the temperature gradient and the airflow, leading to minimal impact on the ARR.
- The CFD model used for simulations may make certain assumptions or simplifications that affect the accuracy of the results.
- The mass flow rates in each section have already been optimized for the given design, minimizing the potential impact of the applied temperature gradients.

Given these considerations, further investigation and analysis, potentially through additional simulations or experiments, may be needed to understand the specific behavior of the receiver and determine if there are opportunities for optimizing its performance.

4.6.3 Mass flow - Temperature Gradient Coupling

The remaining question concerns to the outcome when the previously acquired data concerning the mass flow gradient and temperature gradient are integrated onto the receiver inlet. As illustrated in the figure, the case involving a 50% mass flow gradient and temperature gradient have been combined.

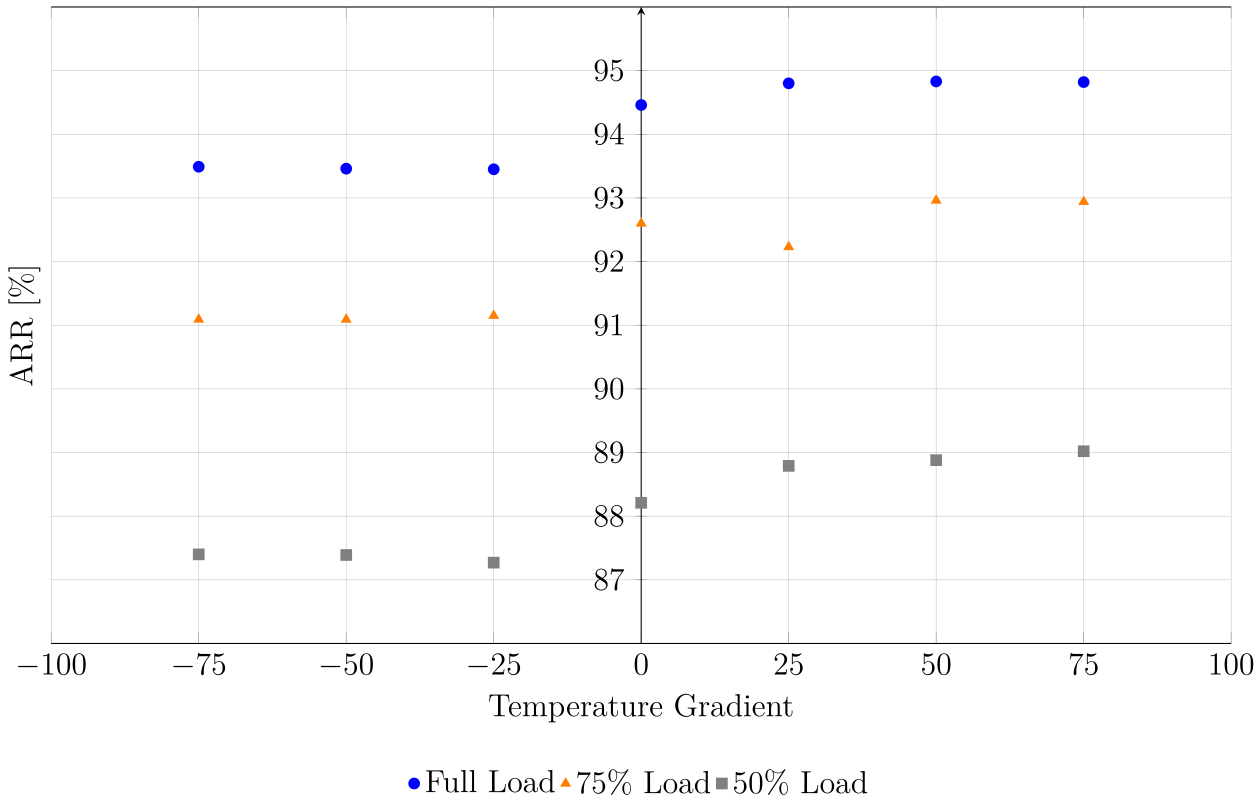

Figure 47: 50% Mass Flow Gradient - Temperature Gradient Coupling

The results exhibit a consistent pattern. Notably, this figure closely resembles the distribution of the mass flow gradient. Thus, it can be inferred that, even with the integration of these distinct gradients, the temperature gradient exerts a minimal impact on the ARR.

5 Potential Analysis and Outlook

5.1 SWOT Analysis

A SWOT analysis will be utilized to evaluate the thesis findings and offer insights into both current and future potential outcomes. This analytical tool aims to provide an objective assessment based on factual data, examining the project's strengths and weaknesses, as well as identifying opportunities and potential threats. Based on the data collected, a SWOT analysis has been undertaken. In conducting this analysis, an emphasis was placed on comprehensively evaluating the internal strengths and weaknesses of the project, along with the external opportunities and potential threats that may impact its success. This process involved a detailed examination of the project's positive attributes, areas that may require improvement and potential challenges that need to be addressed. The aim was to provide a well-rounded assessment.

Strengths:

- **High convergence rate models:** a CFD model of the new cavity receiver used for the integration of the mass flow and temperature gradient of return air flow was created. The model is characterized by an exceptional convergence rate, which is approximately 10 times faster than the original model. The number of iterations reduced from about 2000 iterations to 200 iterations, demonstrating its efficiency in rapidly reaching stable and accurate solutions.

- **Optimized aperture depth of the new concept receiver for high-temperature solar heating:** the receiver configuration, featuring a depth of 150 mm, exhibited the highest ARR, achieving almost 95%, along with efficient convective performance under full load conditions (0.07 kg/s). This suggests a carefully selected geometric design that contributes to improved overall efficiency.

- **Effective mass flow gradient implementation into the inlet surface of absorbers:** implementation of an effective mass flow gradient involves gradually raising or decreasing the mass flow gradient while maintaining a constant total incoming mass flow in receiver model simulations. The findings indicate that increasing the mass flow in proximity to the main absorber leads to higher ARR, with an observed increase of approximately 1.5%. This indicates that no additional equipment or treatment is required to equalize the flow for the returned inlet air to optimize the receiver. The receiver design also maintains effectiveness across varying load levels (full load, 75% load, 50% load). This suggests a robust and adaptable design capable of handling different operational conditions.

- **Limited impact of temperature gradient:** the applied temperature gradients (25°C, 50°C, and 75°C) appear to have little effect on ARR. This suggests that the receiver may not be very sensitive to changes in temperature gradients, potentially raising its adaptation to different conditions. This study shows that there is independence between the calculation of convective losses and irradiance distribution in a CFD model of a cavity solar receiver.

Weaknesses:

- **Limited flow analysis:** the model lacks a comprehensive calculation environment for the complete solar tower system. As a result, it does not analyze the flows in the pipelines, turbines etc. Only the flow within the receiver is examined.

Opportunities:

- **Profitable design:** exploring different operating conditions and absorber materials could uncover new opportunities for performance enhancement and lead to more profitable receiver designs.

- **High temperature potential:** developing a distinct simulation model for the same design of the receiver that would allow a more complex analysis by integrating additional complex simulations, such as incorporating irradiation could be generated. This approach will allow to find the boundary conditions under which the receiver will operate with the maximum temperature potential.

Threats:

- **Limitations of simulation tools:** the accuracy of CFD simulations relies on the precision of the model and the assumptions made. There may be factors or complexities not accounted for in the simulations that could impact real-world performance.

- **Manufacturability and cost considerations:** while the design is effective in simulations, practicality, manufacturability, and potential cost implications should be carefully evaluated to ensure feasibility for real-world implementation.
- **Regulatory and safety compliance:** ensuring that the receiver design adheres to all relevant safety and regulatory standards is crucial for successful deployment and operation.

In summary, the current receiver design exhibits strengths in aperture depth selection and mass flow gradient optimization. However, further exploration of temperature gradient effects, a broader range of aperture depth variations, and practical considerations will be important for refining the design and ensuring its viability for real-world applications.

6 Conclusion

The study investigated two distinct approaches for the first approach was developed to find an optimal geometric variation for the receiver in terms of efficiency and subsequently, the aim of the second approach has been to analyze the influence of both mass flow and temperature gradients on it.

To carry out the analyses, specialized models were generated and evaluated within the ANSYS environment for the two distinct approaches. Given the relatively straightforward geometry, a structured mesh was chosen for its compatibility with such configurations. The k-omega-SST turbulence model was deemed the most suitable, considering the complexity of the flows involved and its advantageous near-wall treatment capabilities. Boundary conditions were selected in alignment with real-world scenarios that ensure accurate and plausible results.

The key metric under investigation was the air return ratio (ARR), which signifies the proportion of air redirected back into the system after being expelled or discharged. Previous research has demonstrated a direct correlation between ARR and receiver efficiency, as a larger proportion of warm air is effectively reused.

Thermal analyses were conducted to optimize the receiver's ARR and efficiency. The results revealed that the depth of the receiver aperture played an important role in increasing ARR. Specifically, transitioning from a depth of 50 mm to 150 mm led to an impressive 7.83% increase in ARR, followed by a 0.3% decrease as the depth reached 200 mm.

Furthermore, assessments of receiver performance encompassed the examination of the rate of change of air inlet mass flow and the response to a rate of change in temperature along the inlet of the receiver. These analyses were conducted in both directions, focusing on both the main absorber and the receiver aperture. The comparative examination of the mass flow gradient reveals that increasing the load condition results in a higher ARR, exerting a more substantial impact compared to the orientation of the applied mass flow gradient. However, altering the loads brings about distinct operational states for the receiver since it leads to different air temperatures.

The direction in which the mass flow gradient is applied becomes notably more influential as the proportion of the gradient is increased. For instance, with a 50% mass flow gradient, an ARR enhancement of 1.4% can be achieved when a higher gradient is applied in proximity to the main absorber. This emphasizes that convective losses are not strongly influenced by mass flow, indicating that adjusting mass flow along the inlet absorber is necessary only for enhancing the mechanical stability of the receiver, specifically to prevent thermal deformation.

Analyses of temperature gradients indicate that introducing such gradients has limited impact on the distribution of ARR under equivalent loads. The applied temperature gradient does affect the flow distribution near the inlet walls but its influence on the internal regions of the receiver is minimal. As a result, it has limited effect on the convective heat losses because it effects on the buoyancy forces and the ARR remain limited. To compute and optimize the overall efficiency of a new solar receiver, it is feasible to separate the computation involving convective losses from other heat losses. This allows for a substantial simplification of the mathematical model for solar collector efficiency for future research.

Upon gathering the collected results, it becomes evident that an observation regarding the ideal configuration of the new receiver concept for high-temperature solar heating and the modes to be employed can be formulated. The receiver attains its highest ARR at full load when possessing a depth of 150 mm. By incorporating a mass flow gradient into the receiver, efficiency can be further elevated by up to 0.21% when the gradient is progressively applied closer to the main absorber.

References

[1] The numerical computation of turbulent flows. *Computer Methods in Applied Mechanics and Engineering*, 3(2):269–289, 1974.

[2] M. Arnold. *Bewertung der Luftrückführung eines offenen volumetrischen Receivers in Cavity-Bauform mit Hilfe von CFD.* PhD thesis, RWTH Aachen, 2017.

[3] N. Belyakov. Chapter seventeen - solar energy. In N. Belyakov, editor, *Sustainable Power Generation*, pages 417–438. Academic Press, 2019.

[4] M. Cagnoli, A. Froio, L. Savoldi, and R. Zanino. Multi-scale modular analysis of open volumetric receivers for central tower csp systems. *Solar Energy*, 190:195–211, 2019.

[5] Y. Cengel and J. Cimbala. Fluid mechanics: Fundamentals and applications. 2014.

[6] A. Cheilytko, F. Göhring, and K. Wieghardt. Receiver efficiency as a determining criterion for the effectiveness of a solar tower. 2022.

[7] A. Cheilytko, P. Schwarzbözl, and K. Wieghardt. Modeling of heat conduction processes in porous absorber of open type of solar tower stations. *Renewable Energy*, 215:118995, 2023.

[8] P. R. Childs. Chapter 2 - laws of motion. In P. R. Childs, editor, *Rotating Flow*, pages 17–52. Butterworth-Heinemann, Oxford, 2011.

[9] M. Drexelius, P. Schwarzbözl, and R. Pitz-Paal. Experimental evaluation of wind induced pressure fluctuations in cavity shaped open volumetric air receivers. *Solar Energy*, 247:146–157, 2022.

[10] J. H. Ferziger and M. Perić. *Computational Methods for Fluid Dynamics*. Springer, Berlin, 2nd edition, 1999.

[11] O. Garbrecht, F. Al-Sibai, R. Kneer, and K. Wieghardt. Cfd-simulation of a new receiver design for a molten salt solar power tower. *Solar Energy*, 90:94–106, 2013.

[12] M. Joardder, P. Halder, M. Rahim, and M. Masud. Chapter eight - solar pyrolysis: Converting waste into asset using solar energy. In M. G. Rasul, A. kalam Azad, and S. C. Sharma, editors, *Clean Energy for Sustainable Development*, pages 213–235. Academic Press, 2017.

[13] X. Ju, C. Xu, Y. Hu, X. Han, G. Wei, and X. Du. A review on the development of photovoltaic/concentrated solar power (pv-csp) hybrid systems. *Solar Energy Materials and Solar Cells*, 161:305–327, 03 2017.

[14] P. S. W. S. S. K. Konrad Busch, Ralf Uhlig and T. Doerbeck. Vocorec - design and performance of the two-stage volumetric conical receiver.

[15] B. Launder and B. Sharma. Application of the energy-dissipation model of flow near a spinning disc. *Lett. Heat Mass Transfer*, pages 131–138, 01 1974.

[16] M. Marcos, M. Romero, and S. Palero. Analysis of air return alternatives for crs-type open volumetric reciever. *Energy*, 29(5):677–686, 2004. SolarPACES 2002.

[17] F. Menter. Zonal two equation kw turbulence models for aerodynamic flows. In *23rd fluid dynamics, plasmadynamics, and lasers conference*, page 2906, 1993.

[18] A. Mills. *Heat Transfer*. Prentice Hall, 2013.

[19] P. Nielsen. 3d cfd-analysis of conceptual bow wings, 2011.

[20] A. K. Pandey, R. K. R., and M. Samykano. Chapter 1 - solar energy: direct and indirect methods to harvest usable energy. In A. K. Pandey, S. Shahabuddin, and M. S. Ahmad, editors, *Dye-Sensitized Solar Cells*, pages 1–24. Academic Press, 2022.

[21] R. Pitz-Paal. 19 - concentrating solar power. In T. M. Letcher, editor, *Future Energy (Third Edition)*, pages 413–430. Elsevier, third edition edition, 2020.

[22] M. Romero and J. González-Aguilar. Solar thermal csp technology. *WIREs Energy and Environment*, 3(1):42–59, 2014.

[23] M. Romero and A. Steinfeld. Concentrating solar thermal power and thermochemical fuels. *Energy Environ. Sci.*, 5:9234–9245, 2012.

[24] H. Stadler, A. Tiddens, P. Schwarzbözl, F. Göhring, T. Baumann, and J. Trautner. Improved performance of open volumetric receivers by employing an external air return system. *Solar Energy*, 155:1157–1164, 2017.

[25] P. Stephan and V. H. Atlas. B1 fundamentals of heat transfer'. *VDI Heat Atlas*, pages 15–30, 2010.

[26] S. Tescari, C. Agrafiotis, S. Breuer, L. Oliveira, M. Neises, M. Roeb, and C. Sattler. Thermochemical solar energy storage via redox oxides: Materials and reactor/heat exchanger concepts. volume 49, 09 2013.

[27] A. Tiddens, M. Röger, H. Stadler, and B. Hoffschmidt. Air return ratio measurements at the solar tower jülich using a tracer gas method. *Solar Energy*, 146:351–358, 2017.

[28] D. Vartziotis, J. Wipper, and M. Papadrakakis. Improving mesh quality and finite element solution accuracy by getme smoothing in solving the poisson equation. *Finite Elements in Analysis and Design*, 66:36–52, 2013.

[29] W. Weiss and F. Mauthner. Solar heat worldwide. *Markets and contribution to the energy supply*, 2010.

[30] G. B. Whitham. An introduction to fluid dynamics. by g. k. batchelor. cambridge university press, 1967. 615 pp. 75s. or 13.50. $JournalofFluidMechanics, 35(3) : 621\breve{}623, 1969.$